COINCIDENCE EXPERIMENTS WITH ELECTRONS *)

W. U. BOEGLIN

Institut für Kernphysik, Universität Mainz, Germany

Received 15 January 1995

Coincidence experiments with electrons provide new information on the structure of nucleons and nuclei. Using new CW accelerators, kinematic regions can be explored with high precision which have not been accessible previously. The equipment and the necessary steps in the analysis of (e,e′p) experiments will be discussed and illustrated with new data taken at the MAMI facility.

Contents

1 Introduction 296
2 The (e,e′p)-reaction 296
3 About CW-beams 299
3.1 CW-beam and duty cycle 299
3.2 Accidental coincidences 300
3.3 CW-accelerator: race track microtron 301
4 Spectrometers 304
4.1 The Mainz three-spectrometer-setup 305
5 Detector system 308
5.1 Vertical drift chambers 309
5.2 Scintillators 311
5.3 Cherenkov detector 311
6 Vertex reconstruction 312
6.1 Determination of θ_0, y_0 and ϕ_0 313
6.2 Determination of δ 315
6.3 Absolute momenta 317
7 Two spectrometer coincidence 318
8 Momentum distribution of deuterium 320
8.1 Experimental details 320
8.2 Phase space considerations 322
8.3 Radiative corrections 326
9 Experimental spectral functions for D, ^{12}C and ^{16}O 327
9.1 Experiments on deuterium 327
9.2 Experiments on ^{12}C and ^{16}O 329
10 Conclusion 332
References 333

*) Lectures given at the Indian-Summer School on Electron Scattering of Nucleons and Nuclei, Prague (Czech Republic), September 1994.

1 Introduction

Electron scattering is an optimal tool for the investigation of the structure of nucleons and nuclei. Its advantage lies in the fact that the electromagnetic interaction is very well described by QED. In addition the interaction between the electron and the nucleus is relatively weak which allows one to probe the inside of a nucleus without strongly disturbing the system. Electron scattering experiments can be separated into two groups. In the first group of experiments one does not observe the final state of the nuclear system, but one 'integrates' over all possible final states. These types of experiments are called inclusive experiments. In the second group in contrast one also detects a second (or third, fourth etc.) particle which has been knocked out or which has been produced in the reaction in coincidence with the scattered electron. These reactions are called exclusive or semi-exclusive reactions since certain possible final states are excluded. Exclusive reactions enable one to study nuclear structure from a point of view where one "takes the nucleus apart" by ejecting nucleons from their bound states and measuring their final momentum. From these reactions one can in the most simple approximation determine the Fourier transform of the wave function of the corresponding nuclear state. Another possibility is to excite individual nucleons and observe their decay by detecting the particles produced in coincidence with the scattered electron. From these reactions one can learn about the dynamical properties of bound nucleons and about the propagation of excited states in nuclear matter. Given enough energy it is also possible to produce particles with strangeness in the nucleus and investigate their behaviour in the nuclear medium. In coincidence reactions additional matrix elements contribute to the cross section which contain information not accessible in an inclusive experiment. For instance, the use of polarized electrons and a determination of the polarization of the emerging nucleons enables one to determine nucleon formfactors. This technique is especially promising for determining the neutron electric formfactor.

With the new CW-beams available, it is now possible to study coincidence reactions with high precision in kinematical regions which have not yet been accessible. In these lectures I will describe the tools, namely spectrometers and their instrumentation, used to perform (e,e′p) experiments at Mainz.

2 The (e,e′p)-reaction

The (e,e′p)-reaction can be viewed schematically as shown in Fig. 1. The virtual photon is absorbed by a bound nucleon having a certain initial momentum p_i, which leaves the nucleus with a kinetic energy T_p. The residual system may remain in its ground or in an excited state and has a recoil momentum p_{miss} (often denoted also as p_r). The transferred energy ω is divided between the kinetic energy of the ejected nucleon, its separation energy and possibly the excitation energy of the residual system. From momentum and energy conservation one can build the missing momentum p_{miss} and the missing energy ϵ_m as follows:

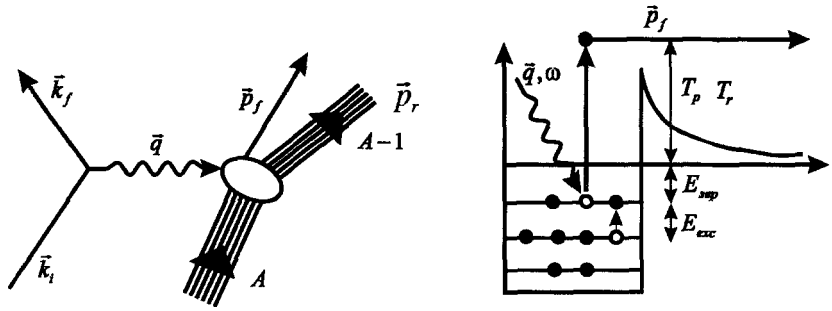

Fig. 1. The (e,e′p) reaction where a bound nucleon is knocked out and leaves the nucleus with a kinetic energy T_p. The residual system can be excited and is recoiling with the kinetic energy T_r.

$$\begin{aligned} &\text{Momentum conservation:} \quad \vec{q} &&= \vec{p}_\mathrm{f} + \vec{p}_\mathrm{miss}\,, \\ &\text{Energy consevation:} \quad \epsilon_\mathrm{m} &&= \omega - T_\mathrm{p} - T_\mathrm{r}\,. \end{aligned}$$

Here T_r is the kinetic energy of the recoiling system.

Assuming one photon exchange, the cross section for a coincidence reaction where one particle is detected in coincidence with the scattered electron can be written as follows [1,2] (Fig. 2):

$$\frac{\mathrm{d}^6\sigma}{\mathrm{d}\omega\mathrm{d}\Omega_\mathrm{e}\mathrm{d}T_\mathrm{p}\mathrm{d}\Omega_\mathrm{p}} = \sigma_\mathrm{Mott}\left(v_\mathrm{L}R_\mathrm{L} + v_\mathrm{T}R_\mathrm{T} + v_\mathrm{LT}R_\mathrm{LT}\cos\phi + v_\mathrm{TT}R_\mathrm{TT}\cos 2\phi\right).$$

The functions R_i and R_{ij} are response functions and consist of combinations of matrix elements of the electromagnetic currents in the system investigated. They are functions of $\vec{q}, \omega, \theta_\mathrm{pq}$ and p_f. The quantities v_i and v_{ij} depend on the electron kinematics only and describe the polarization of the virtual photon. If the ejected particle is observed in the direction of $\vec{q}$ (parallel kinematics), the interference response functions R_{ij} vanish and the remaining response functions can be separated by varying the electron scattering angle and the incident energy in order to keep

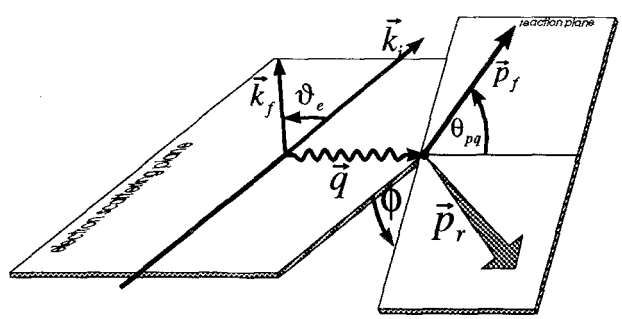

Fig. 2. The relevant kinematic variables which enter the general expression for the (e,e′p) cross section.

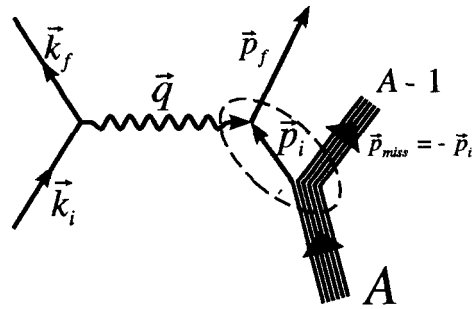

Fig. 3. The (e,e′p) reaction as viewed in PWIA.

all the remaining kinematic variables constant (Rosenbluth separation). The determination of R_{TT} requires a detection of the emerging particle out of the electron scattering plane. The separation of response function constitutes a large part of the experimental programs at the new facilities.

In the simplest approximation to describe this reaction, the nucleon is assumed to be free after it has absorbed the virtual photon. It leaves the nucleus without any further interaction and can be described by a plane wave. The struck nucleon is detected in coincidence with the scattered electron. These are the assumptions of the Plane Wave Impulse Approximation (PWIA) (Fig. 3). In this approximation the recoil momentum of the residual system is antiparallel to the inital momentum of the struck nucleon. The cross section can be written as follows:

$$\frac{\mathrm{d}^6\sigma}{\mathrm{d}\omega\mathrm{d}\Omega_{\mathrm{e}}\mathrm{d}\Omega_{\mathrm{p}}\mathrm{d}T_{\mathrm{p}}} = K \cdot \sigma_{\mathrm{ep}} \cdot S(E, p_{\mathrm{i}})\,.$$

Here σ_{ep} describes the elementary electron proton (off shell) cross section for scattering an electron off a moving (bound) nucleon [4]. The factor K is a kinematical factor (in this case $K = p_{\mathrm{f}}E_{\mathrm{p}}$) and $S(E, p_{\mathrm{i}})$ is the spectral function which describes the probability of finding a proton with the separation energy E and an inital momentum p_{i}. For a bound hole state of the residual system the spectral function is a delta function in the missing energy. As a function of the missing momentum the spectral function for this bound state corresponds in the independent particle shell model to the Fourier transform of its wave function. In reality the emerging nucleon does interact with the residual nucleus and its wave function is not a plane wave any more. In this case $\vec{p}_{\mathrm{f}} \neq -\vec{p}_{\mathrm{miss}}$ and the spectral function has to be replaced by the distorted spectral function $S_{\mathrm{dist}}(E, \vec{p}_{\mathrm{miss}}, \vec{p}_{\mathrm{f}})$. The final state interaction (FSI) for a heavy nucleus is described by means of an optical potential. This approach corresponds to the distorted wave impulse approximation (DWIA) [2]. In both approximations the electron waves have been described by plane waves which is not valid for heavy nuclei [3].

In the following sections I will describe the equipment and the basic steps in order to determine an (e,e′p) cross section and from it the momentum distribution.

3 About CW-beams

In the past coincidence experiments with electrons have been very difficult to perform due to the smallness of the cross sections involved and due to the very high instantaneous rates in the detectors. These high rates are a consequence of the low duty cycle of the electron accelerators available at that time.

3.1 CW-beam and duty cycle

Linear electron accelerators with energies of typically up to 1 GeV, as are in operation at NIKHEF, BATES or Saskatoon, produce a pulsed electron beam. The beam has a repetition rate of typically 500 to 1000 Hz and a peak current of about $I_{\text{peak}} = 5$ mA in one beam pulse. This is schematically shown in Fig. 4 (left). The

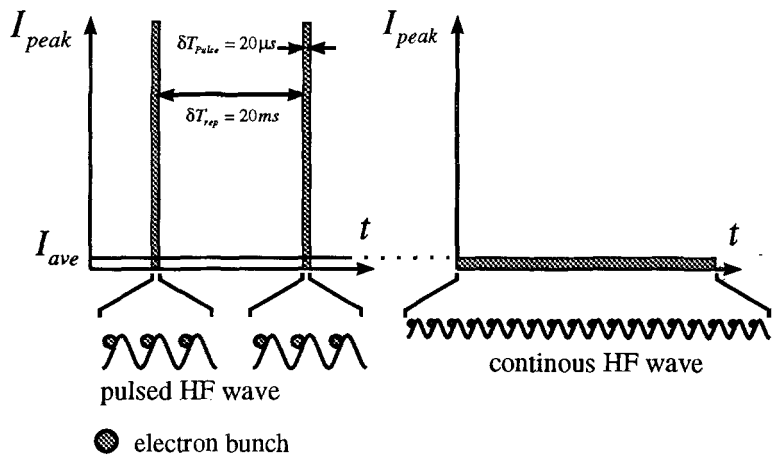

Fig. 4. The time structure of a pulsed electron beam(left). The pulse length is $\delta T_{\text{pulse}} = 20\,\mu$s and the repetition period (time between pulses) is $\delta T_{\text{rep}} = 20$ ms. Right: time structure of a CW (continous wave) beam, every HF wave is loaded with a bunch of electrons in contrast to the pulsed machine where the waves are loaded during the pulse length only. Note that a CW-beam is not a DC beam as one would obtain from a van-de-Graaf accelerator for instance.

ratio between pulse length and repetition period $\tau = \delta T_{\text{pulse}}/\delta T_{\text{rep}}$ is called the duty cycle. An accelerator with a duty cycle of 1% and a peak current of 5 mA produces consequently an average current of $I_{\text{average}} = I_{\text{peak}} * \tau = 50\,\mu$A.

In contrast a CW-beam (CW = Continous Wave) has besides its microstructure no pulsed structure. The micro structure is a consequence of the high frequency electric field which is used in the accelerating cavities of the accelerator and is also pertinent in the beam pulse of a pulsed machine. If the time resolution of the detection system is larger than the length of a micro pulse, the peak current of a CW-beam is therefore equal to its average current (see Fig. 4 right).

3.2 Accidental coincidences

The importance of a CW-beam becomes clear if one studies the ratio between the coincidence rate and the accidental rate. The time sequence of events in two detectors is shown schematically in Fig. 5. The "coincidence gate" is opened by detector

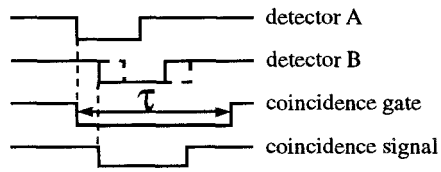

Fig. 5. Timing of events from different detectors.

A (e.g. the electron spectrometer) and has a length of τ seconds which is called the coincidence time. The signal which opened the coincidence gate could have been a particle from the investigated coincidence reaction (e.g. (e,e'p)) or some other reaction (e.g. (e,e'n)) which does not produce any secondary particles which could be detected by detector B (e.g. the proton spectrometer). A real coincident particle would produce a signal in detector B, with a fixed time relation to the signal in detector A, while an uncorrelated particle would arrive at any time with respect to the particle detected in detector A. If one histograms the time between the signal in detector A and B, one would consequently observe a peak for the coincidences and a flat backgound for the accidental coincidences. The flat background should be as wide as the coincidence gate. In order to identify and isolate the true coincidences from the background of accidental ones it is important that the ratio of true coicidences to accidental coincidences should be as large as possible. This ratio is often called the signal-to-noise ratio. As an example I use the (e,e'p) reaction. The event rate in the electron detector is $\dot{N}_{\mathrm{e}}$ and in the proton arm it is $\dot{N}_{\mathrm{p}}$. The coincidence time is τ. I assume now that the electron arm opens the coincidence gate. During a time period of Δt seconds it is therefore open for $\Delta T = \tau \cdot \dot{N}_{\mathrm{e}} \cdot \Delta t$ seconds. In this time period the other detector observes, on the average, the number of accidentals of $N_{\mathrm{acc}} = \Delta T \cdot \dot{N}_{\mathrm{p}}$ events. The rates $\dot{N}_{\mathrm{e}}$ and $\dot{N}_{\mathrm{p}}$ are the instantaneous rates, i.e., the rates the detectors are exposed to when the beam is on the target:

$$\dot{N}_{\mathrm{e}} = C_{\mathrm{e}} \cdot I_{\mathrm{peak}} = C_{\mathrm{e}} \cdot \frac{I_{\mathrm{ave}}}{f_{\mathrm{d}}},$$

$$\dot{N}_{\mathrm{p}} = C_{\mathrm{p}} \cdot I_{\mathrm{peak}} = C_{\mathrm{p}} \cdot \frac{I_{\mathrm{ave}}}{f_{\mathrm{d}}}.$$

Therefore $\dot{N}_{\mathrm{acc}} = C_{\mathrm{e}} \cdot C_{\mathrm{p}} \cdot I_{\mathrm{ave}}^2 / f_{\mathrm{d}}^2$ depends quadratically on the beam intensity and duty factor f_{d}. For the coincidence rate one obtains $\dot{N}_{\mathrm{coin}} = C_{\mathrm{coin}} \cdot I_{\mathrm{ave}}/f_{\mathrm{d}}$. The signal-to-noise ratio can now be calculated :

$$\frac{\dot{N}_{\mathrm{coin}}}{\dot{N}_{\mathrm{acc}}} = \frac{C_{\mathrm{coin}}}{C_{\mathrm{e}} \cdot C_{\mathrm{p}}} \cdot \frac{f_{\mathrm{d}}}{I_{\mathrm{ave}}}.$$

It becomes clear that the difference between a duty factors of 0.01 and 1 corresponds to a factor of 100 in the signal-to-noise ratio and a to factor of 10000 in the accidental rate at the same beam intensity. The signal to noise ratio also determines the number of coincidences which have to be collected in the coincidence window in order to obtain a certain statistical precision. The true coincidences are defined in a rather arbitrary way by means of a cut on the coincidence time (Fig. 6) which is usually set to about three to four times larger than the FWHM of the coincidence peak in order to avoid loss of real coincidences due to the cut. The number of events within this cut (Fig. 6, shaded area) are called true coincidences

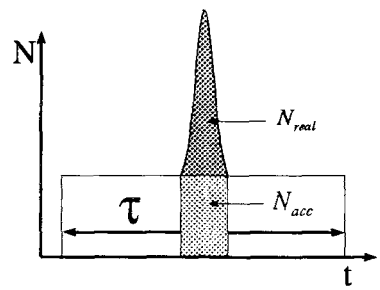

Fig. 6. The coincidence time spectrum and the coincidence window.

$N_{\text{true}} = N_{\text{real}} + N_{\text{acc}}$. From the true coincidences one has to subtract the accidental coincidences. One obtains for the relative error in the real coincidences N_{real} the following expression:

$$\frac{\Delta N_{\text{real}}}{N_{\text{real}}} = \frac{1}{\sqrt{N_{\text{real}}}}\sqrt{1+\frac{1}{\lambda}}$$

where $\lambda = N_{\text{real}}/N_{\text{acc}}$ is the signal-to-noise ratio. As a consequence the smaller the signal-to-noise ratio the larger is the number of real coincidences required and therefore the larger is the beam time requirement. Therefore a CW-beam allows one to study reactions which have been impossible to study up to now due to the smallness of the cross section.

3.3 CW-accelerator: race track microtron

Linear accelerators which are in use at BATES and NIKHEF have a typical length of 200 m and a total energy of about 400 MeV and consist of about 20 to 30 accelerating sections. In each section the particle gains about 10 MeV. The high voltage gradients in these structures produce very high currents in the walls of the cavities and produce therefore very large losses (i.e. they heat the cavity). This is the reason why these accelerators are operated in a pulsed mode where the high frequency power is applied to the accelerating section for a very short time only, producing the short and very intense beam pulse. In order to produce a continous beam, the accelerating sections have to be continously supplied with HF power. This is only possible if either the accelerating gradient is small or if

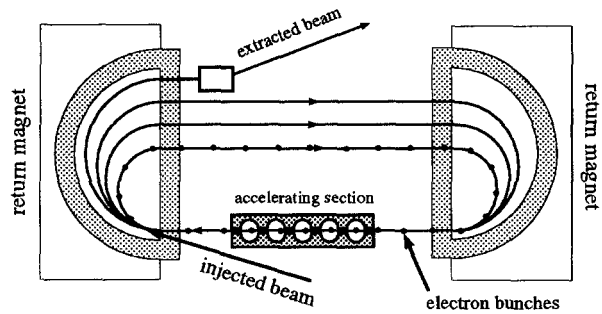

Fig. 7. Principle of the race track microtron.

the resistance of the cavities is dramatically reduced. A linear accelerator with a small gradient, however, would become very long and impracticable. The race track microtron circumvents [5] this problem by accelerating the electron with the same small linear accelerator. It is shown schematically in Fig. 7.

Electrons are injected into the linac of the microtron and gain a certain amount of energy. From the linac and some focusing elements they enter a homogenous magnetic field and are deflected by 180°. From a field free drift region the electrons

Table 1. The main parameters of the Mainz Microtron MAMI.

RTM		I	II	III
General Data				
input energy	MeV	3.5	14	180
output energy	MeV	14	180	≤ 855
linac traversals		20	51	90
Magnets				
distance between magnets	m	1.67	5.6	12.8
flux density	T	0.10	0.56	1.28
diameter of max. orbit	m	0.97	2.17	4.43
Linacs				
number of klystrons		1	2	5
(electrical) linac length	m	0.8	3.55	8.87
total r.f. power	kW	9	65	168
beam power	kW	1.1	17	66
energy gain per pass	MeV	0.60	3.24	7.5
Beam				
current	μA	≤ 100		
energy	MeV	180–855 in steps of 15 MeV		
energy width (FWHM)	keV	18	36	120
emittance vertical	$\pi \cdot$ mm $\cdot$ mrad	0.17	0.014	0.001(25)
emittance horizontal	$\pi \cdot$ mm $\cdot$ mrad	0.17	0.014	0.007(25)

enter another homogenous magnetic field and enter again the linac to be further accelerated. Each time an electron has passed through the linac it uses another track on the return path. This procedure is repeated until the electrons have gained enough energy and encounter the extraction magnet which allows them to leave the microtron. The condition for the operation of the microtron is as follows:

- $v_e \approx c$, where v_e is the speed of the electrons,
- the magnetic field $\vec{B}$ and the energy gain ΔE have to be such that the time difference $\Delta t = t_{i+1} - t_i$ is a multiple n of the high frequency period

$$\Delta E = n \frac{ec^2 B}{2\pi \nu_{\mathrm{HF}}} .$$

For a magnetic field of 1.28 T and a $\nu_{\mathrm{HF}} = 2.449$ GHz and $n = 1$ one obtains $\Delta E = 7.5$ MeV (these are the parameters for RTM3, see below).

The accelerator system at Mainz consists of a linear accelerator which produces relativistic electrons and a series of 3 race track microtrons which produce a max-

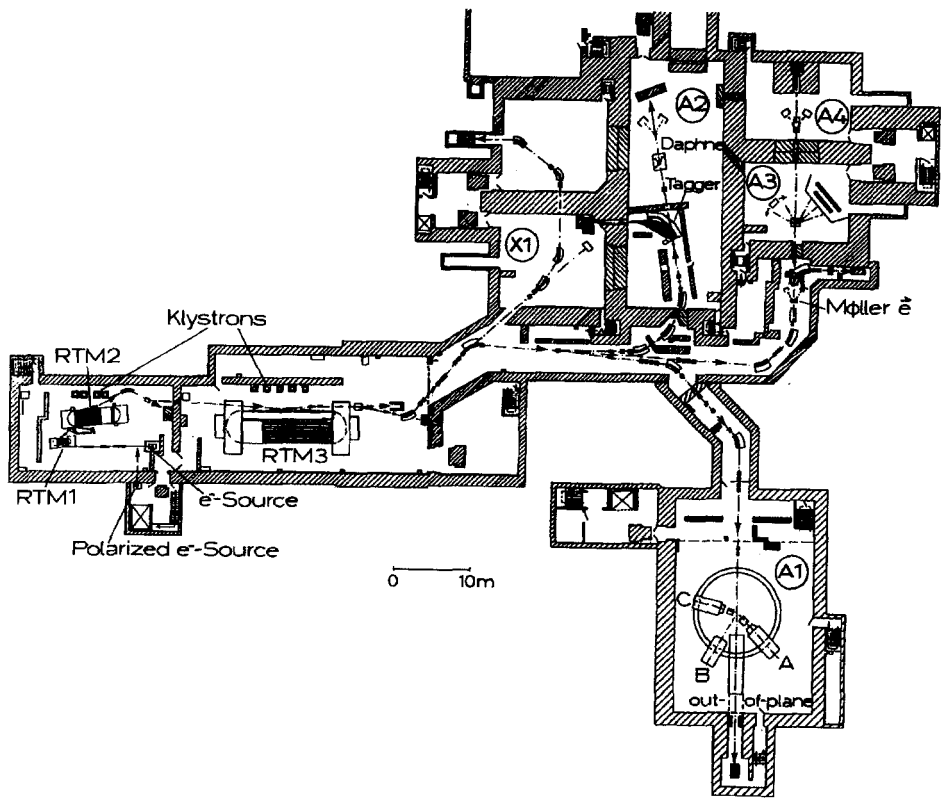

Fig. 8. The Mainz Microtron facility with the experimental halls.

imum energy of 855 MeV and a maximum current of 100 μA. The parameters of these accelerators are shown in Table 1. The arrangement of the different accelerators and the experimental halls is shown in Fig. 8.

At MAMI [5] one uses accelerating sections with rather low field gradients which allows one to operate the cavities continuously and to produce therefore a beam with a duty factor of 100%.

An electron accelerator which uses superconducting cavities has just delivered its first beam this summer at the Continous Electron Beam Accelerator Facility (CEBAF) in Virginia. This facility consists of two linear superconducting accelerators with an energy gain per pass and per accelerator of about 400 MeV. The system is designed for 5 passes which corresponds to a maximal beam energy of 4 GeV. For further detail see reference [6].

Another scheme to convert the beam of a pulsed linear accelerator into one with a duty factor of about 100% is to use a pulse stretcher ring. This scheme is employed at NIKHEF(AMPS) [9] at BATES(SHR) [10] and Saskatoon [11].

4 Spectrometers

A precise determination of relevant kinematical quantities, such as momentum transfer, energy transfer, missing momentum etc. requires detection systems which are capable of determining the 4-vectors of the observed particles. This is achieved by means of magnetic spectrometers. The optical properties of a spectrometer can be calculated by solving the equation of motion of a charged particle in a given magnetic field configuration:

$$\dot{\vec{p}} = q(\dot{\vec{r}} \times \vec{B}) .$$

For the type of spectrometers used in Mainz the magnetic field has the following properties:

- between the pole faces, $\vec{B}$ can be described as the gradient of a scalar field $\vec{B} = -\nabla\Phi$ which fulfills the Laplace equation $\triangle\Phi = 0$.
- in the magnetic system there exists a symmetry plane around which one component (usually the y-component) of the magnetic field is symmetric (this corresponds to an equipotential plane). At the symmetry plane which is called the magnetic midplane, the field is perpendicular to it.
- the magnet pole faces are arranged symmetrically around the magnetic midplane.
- the scalar potential Φ is an odd function of y:

$$\Phi(x, y, z) = -\Phi(x, -y, z) .$$

Since the scalar field Φ fulfills the Laplace equation the field $\vec{B}(x, y)$ is determined if one of the components, e.g. $B_y(x, y)$, is given as a function of one of the coordinates

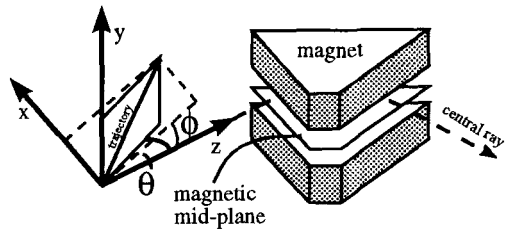

Fig. 9. The magnetic midplane and the coordinate system used.

x, or y, e.g. $B_y(x, y = 0)$. The magnetic field component B_y can be expressed as a series of multipoles:

$$B_y(x) = B_{y0} + \frac{\partial B_y}{\partial x} x + \frac{1}{2!} \frac{\partial^2 B_y}{\partial x^2} x^2 + \cdots .$$

The lowest multipoles such as dipole B_{y0} and quadrupole $\partial B_y / \partial x$ are the elementary building blocks of particle optical systems since they play the same role as prisms and lenses in light optics. They can be realized as separated devices. Higher multipoles are used to correct for aberrations and are frequently included into the discrete elements (e.g. curved pole faces of dipole magnets produce sextupole strength). A detailed discussion of the equation of motion and the relation to particle optics can be found in reference [12]. Standard computer codes for these calculations are programs like TRANSPORT [14] or RAYTRACE [13].

4.1 The Mainz three-spectrometer-setup

An overview of the spectrometer setup [16] used in Mainz is shown in Fig. 10. Two of the spectrometers (called A and C) are QSDD-spectrometers, which means that their optical system consists of the elements quadrupole(Q), sextupole(S), dipole(D) and another dipole(D) (Fig. 11). The first quadrupole is used to obtain a large solid angle by providing transverse focusing. The two dipoles generate the dispersion and the focusing. The polefaces of the dipole magnets are inclined which introduces additional quadrupole strength. The sextupole magnet is mainly used to correct for spherical aberrations in the non dispersive plane. Both spectrometers are point-to-point focusing in the dispersive plane for optimal momentum resolution and are parallel-to-point focusing in the transverse (non dispersive) plane for optimal angle determination. As a consequence of the parallel-to-point optics the position resolution in the transverse plane is reduced. This lack of resolution is compensated by spectrometer B which is a clam shell spectrometer (Fig. 12). This spectrometer consists of one dipole magnet only. Its field has a gradient which provides transverse focusing and the entrance and exit pole faces are inclined to provide quadrupole and sextupole strength. In contrast to the other two spectrometers it has a smaller solid angle and a reduced momentum acceptance. However, it is very compact and has point-to-point focusing in both planes. Therefore it has a very good momentum resolution in combination with a very good position resolution. This makes it an

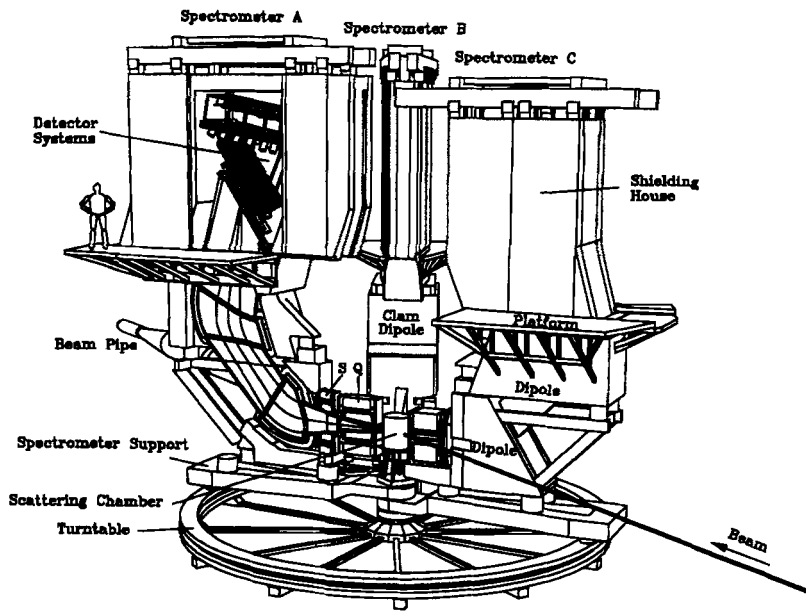

Fig. 10. Overview of the three-spectrometer-setup.

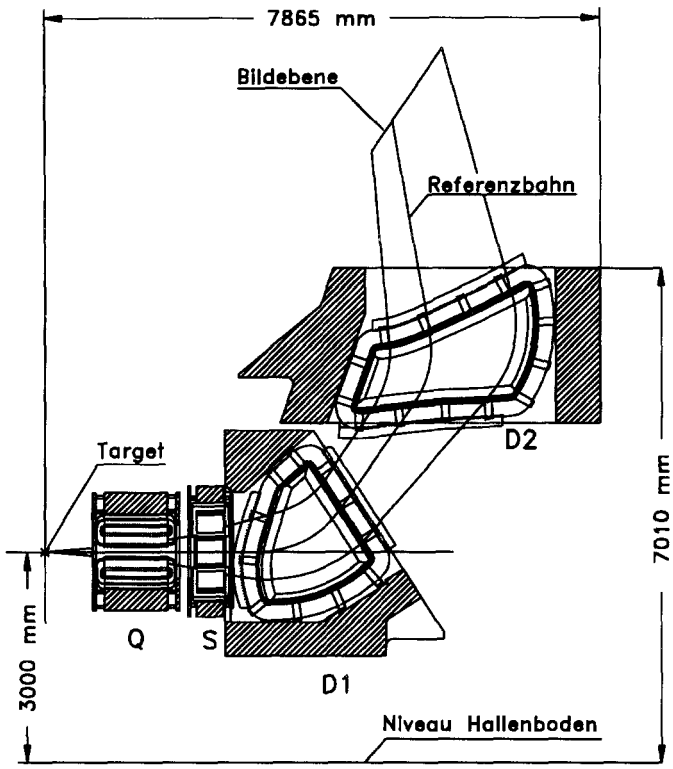

Fig. 11. Cross section of the QSDD spectrometer A. One can clearly see the inclined and curved pole faces which produce magnetic field components up to eights order.

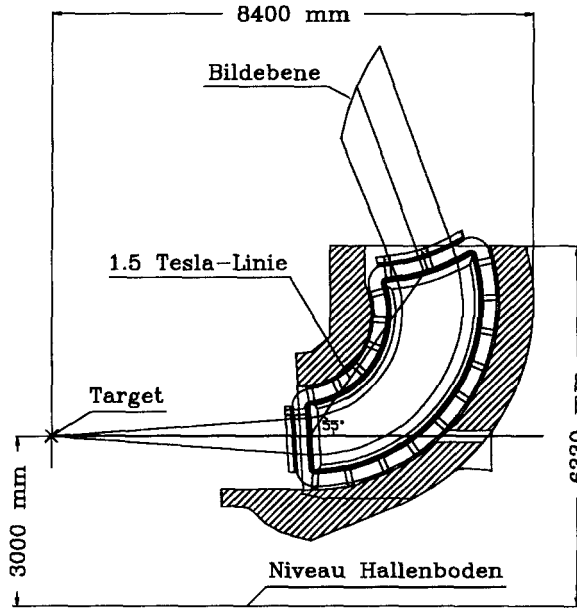

Fig. 12. The clam shell spectrometer B which has a field gradient transverse to the midplane.

ideal partner to one of the other spectrometers. In addition due to its compactness it is able to detect particles with scattering angles as small as 7° with respect to the electron beam. This is very important for performing R_L/R_T separations at high missing momenta. This spectrometer can also be moved vertically by 10° which allows one to perform out-of-plane experiments with a high resolution instrument. In Table 2 an overview over the main parameters characterizing the spectrometers is given. The optical properties of all spectrometers have been optimized to achieve a straight image plane inclined by 45° to the reference trajectory with minimal spherical and higher momentum dependent aberrations.

5 Detector system

The detector system has two main tasks to accomplish. One is to determine the trajectory coordinates (x, θ, y, ϕ) with an accuracy that matches the optical properties of the spectrometers. The other task is to identify the detected particles in order to separate the investigated reaction type from possible background reactions. In addition the detection package also provides a timing signal for a detected particle which is used internally and in coincidence with another detector. All three spectrometers at Mainz have a similar detection system. Figure 13 shows the focal plane instrumentation of spectrometer A.

Table 2. Main parameters of the three spectrometers. Note that vertical means in the dispersive plane and horizontal means transverse to the dispersive plane.

Spectrometer Configuration		A QSDD	B D	C QSDD
Maximum momentum	MeV/c	735	870	551
Maximum induction	T	1.51	1.50	1.40
Momentum acceptance	%	20	15	25
Solid angle	msr	28	5.6	28
Horizontal acceptance	mr	±100	±20	±100
Vertical acceptance	mr	±70	±70	±70
Long-target acceptance	mm	50	50	50
Scattering angle range	°	18–160	7–62	18–160
Length of central trajectory	m	10.75	12.03	8.53
Dispersion (central trajectory)	cm/%	5.77	8.22	4.52
Magnification (central trajectory)		0.53	0.85	0.51
Dispersion to magnification	cm/%	10.83	9.64	8.81
Momentum resolution (measured)		2×10^{-4}	1×10^{-4}	1×10^{-4} [a])
Angular resolution at target	mrad	≤ 3	≤ 3	≤ 3
Position resolution at target (FWHM)	mm	6	1.5	6

[a]) design

5.1 Vertical drift chambers

Two Vertical Drift Chamber (VDC) packages are used to determine the trajectory coordinates of the particle in the focal plane. Each package detects the x- and the y-coordinate of the trajectory in the corresponding wire plane. The principle operation of a VDC is illustrated in Fig. 14 [18]. A series of parallel wires is positioned between two parallel conducting planes which are at high voltage (typically at 6.5 kV). The space between the high voltage planes is filled with a gas mixture (e.g. 50% isobutane 48% argon and 2 % ethanol). The electric field lines are mainly perpendicular to the wire plane except in the vicinity of a wire. The electron clouds produced by a particle along its path through the chamber drift along the field lines to the anode wires. Very close to one of these wires the electric field is strong enough that the electron can ionize other atoms or molecules of the gas and produce secondary electrons. This process results in an avalanche located close to the wire. The primary ionization is therefore amplified with a gain typically of the order of 10^6. By measuring the drift time for these electrons and with the knowledge of the drift time to drift distance conversion (which can be determined experimentally) one obtains the location where the particle trajectory crossed the different drift cells. In spectrometer A on the average 4 to 5 drift cells are crossed by a trajectory. Via a linear fit one determines the location x in the wire plane and the angle θ of the trajectory with respect to the wire plane. Combining two such wire planes where the wires in one plane are rotated by an angle ϕ_w with respect to the wires in the other plane it is possible to determine the x- and the y-coordinate of the

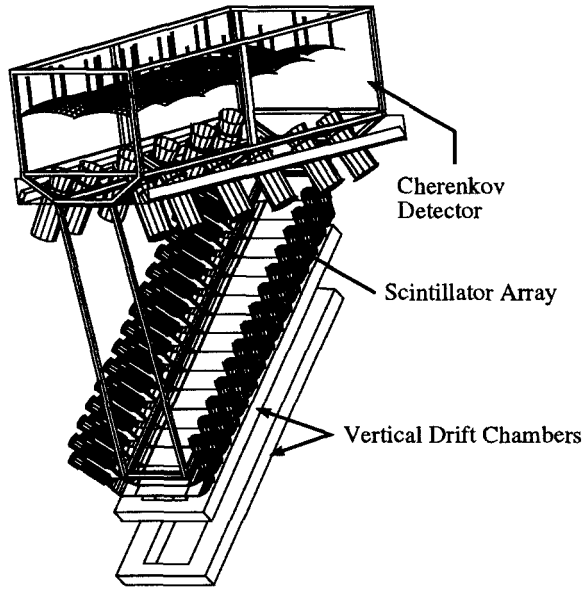

Fig. 13. Focal plane detector system of spectrometer A. The trajectory coordinates are determined by two sets of vertical drift chambers (VDC). The VDC's are followed by two layers of plastic scintillators which provide the timing signals for the VDC's and the coincidence setup. The signal height information is used for particle identification. The scintillator array is followed by a gas Cherenkov detector used for electron identification.

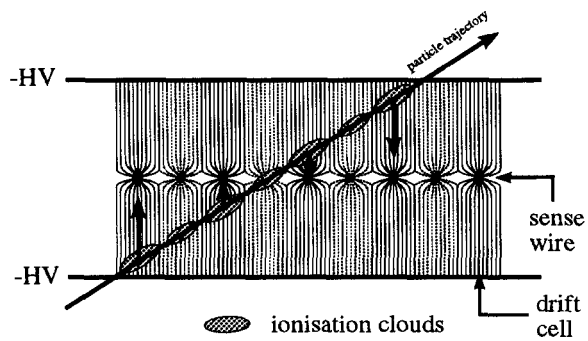

Fig. 14. Operation principle of a VDC.

trajectory in the corresponding plane. The angle ϕ_w is usually of the order of 45°. The position resolution in one plane is typically 0.2 mm (FWHM). With two such chamber packages one can then determine position and direction of a particle trajectory with an averaged resolution given in Table 3. The efficiency of the chambers has been determined to be better than 99%.

Table 3. Accuracy of the trajectory determination in the focal plane of spectrometer A averaged over the active area of 222×40.5 cm^2.

Δx	0.2 mm (FWHM)
$\Delta\theta$	0.5 mrad (FWHM)
Δy	0.4 mm (FWHM)
$\Delta\phi$	3 mrad (FWHM)

5.2 Scintillators

As shown in Fig. 13 the VDC's are followed by two layers of plastic scintillation detectors (Fig. 15). Each plane contains about (depending on the spectrometer) 14

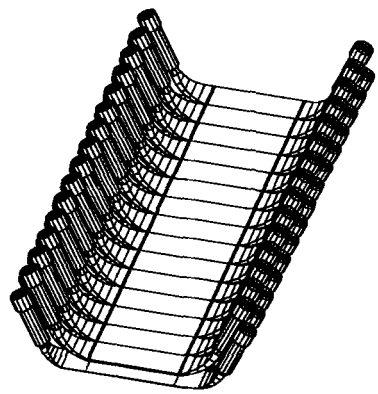

Fig. 15. Scintillator array of spectrometer A.

individual detectors with 2 photomultipliers at each end. This has the advantage of a very good time resolution over a large detection area since the path lengths of the light in the scintillation material is kept short. In addition the segmentation of the large detection area reduces the background rates. In the first layer the scintillators are thinner (3 mm) than the ones in the second one (10 mm) in order to allow a particle identification via measurement of the differential energy loss of the different paricles which pass with different velocities. This measurement is mainly used to separate pions and positrons from protons. A separation between electrons and pions is not possible since the pions are in most cases minimum ionizing particles like the electrons and the difference in their energy loss is too small to be observed.

5.3 Cherenkov detector

A gas Cherenkov detector which follows the scintillation detectors is used to discriminate between electrons and pions (minimum ionizing particles for $p_\pi > 200\,\mathrm{MeV}/c$). This detector is filled with freon gas (freon 114) which gives an optical

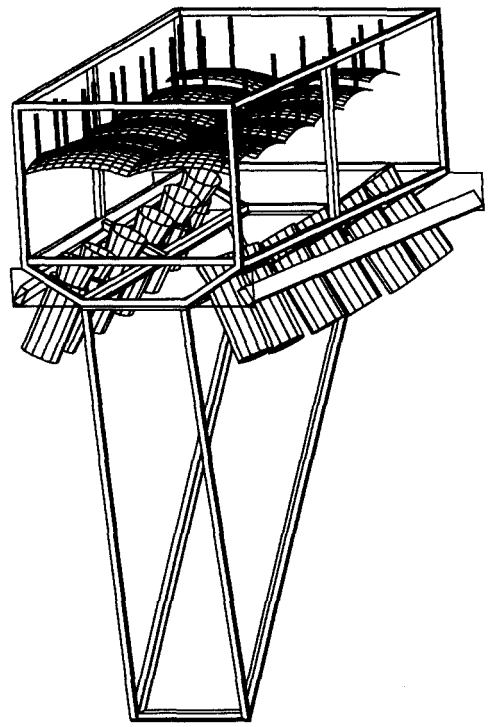

Fig. 16. Cherenkov detector of spectrometer A.

medium with an index of refraction very close to one (1.0013). Cherenkov light is emitted if a charged particle passes a material with a speed larger than the speed of light in the material. Light emmission occurs at an angle $\theta_{\check{C}}$ which is determined by $\theta_{\check{C}} = \arccos 1/\mathrm{n}\beta$ where n is the index of refraction of the radiator. For the detector of spectrometer A, electrons with a momentum $p_e > 10$ MeV/c produce a signal and pions would need a momentum of $p_\pi > 2700$ MeV/c in order to cross the threshold. For a particle with a velocity such that $\beta n \approx 1$ the radiation is essentially emitted parallel to the particle trajectory. The Cherenkov detector installed in spectrometer A is shown in Fig. 16. Mirrors in combination with light collecting "funnels" at the entrance of the photomultipliers are used in order to collect as many Cherenkov photons as possible to cover the large angular range of the particle trajectories with respect to the reference (central) trajectory. The efficiency of the Cherenkov detector has been determined to be about 99.98%.

6 Vertex reconstruction

From the measured trajectory coordinates in the focal plane, one has to determine the trajectory coordinates at the target. This poses a fundamantal problem because a trajectory at the target is characterized by five quantities $x_0, \theta_0, y_0, \phi_0$

and δ. In the focal plane, however, one can only measure four quantities x, θ, y and ϕ. It is therefore necessary to set one of the target coordinates to a known value for all trajectories which enter the spectrometer, this is usually the x_0 coordinate which is set to zero by focusing the beam to a small spot on the central trajectory of the spectrometer. From the four coordinates in the focal plane one can then determine the remaining four coordinates at the target. In first order optics this could be done by simply inverting the transfer matrix. For a more realistic optical system including aberrations the inversion procedure becomes more involved. Even if the system can be theoretically described very accurately by higher order optics one needs a detailed knowledge of the magnetic field including the fringe field regions in order to calculate the target coordinates from the given focal plane ones. The required field maps are usually not available for the completed system. There are several different methods available to solve this problem. For instance, a careful treatment can be found in Refers. 17 and 19. In the following I will describe the basic steps in experimentally determining the inversion function (often called the reconstruction matrix and dispersion formula) described in reference [20].

6.1 Determination of θ_0, y_0 and ϕ_0

Generally a quantity q at the target is labeled with the index "tg", e.g. $\theta_{\rm tg}$, while a quantity in the focal plane is labeled with the index "fp", e.g. $\theta_{\rm fp}$. One describes the dependency of $q_{\rm tg}$ on $q_{\rm fp}$ in terms of a general polynomial of the form:

$$q_{\rm tg} = \sum_{jkl} Q^q_{jkl} \theta^j_{\rm fp} y^k_{\rm fp} \phi^l_{\rm fp}$$

with

$$Q^q_{jkl} = \sum_i \langle q_{\rm tg} | x^i_{\rm fp} \theta^j_{\rm fp} y^k_{\rm fp} \phi^l_{\rm fp} \rangle x^i_{\rm fp} \, .$$

The expression Q^q_{jkl} which is the coefficient in the polynomial in the variables $\theta_{\rm fp}, y_{\rm fp}$ and $\phi_{\rm fp}$ is itself a polynomial in the focal plane coordinate $x_{\rm fp}$ with the coefficients $\langle q_{\rm tg} | x^i_{\rm fp} \theta^j_{\rm fp} y^k_{\rm fp} \phi^l_{\rm fp} \rangle$ for each power in $x_{\rm fp}$. This notation turns out to be useful for the experimental determination of these coefficients as will be seen below. In order to determine these terms one uses a sieve slit detector as shown in Fig. 17. This collimator defines a bundle of electron beams which enter the spectrometer at known angles without any loss of energy or multiple scattering. Using elastic electron scattering from a heavy nucleus (e.g. Ta), one can identify the holes in the two dimensional spectrum $\theta_{\rm fp}$ versus $y_{\rm fp}$ for spectrometer A (Fig. 18). As an example I want to discuss the determination of the coefficients to reconstruct the angles $\phi_{\rm tg}$ and $\theta_{\rm tg}$. For a given set of starting values for $\langle \theta_{\rm tg} | x^i_{\rm fp} \theta^j_{\rm fp} y^k_{\rm fp} \phi^l_{\rm fp} \rangle$ and $\langle \phi_{\rm tg} | x^i_{\rm fp} \theta^j_{\rm fp} y^k_{\rm fp} \phi^l_{\rm fp} \rangle$ one determines the quantity (for $\theta_{\rm tg}$) :

$$\Delta\theta = \sum_s \left[\frac{\sum_{jkl} Q^\theta_{jkl} \theta^j_{\rm fp} y^k_{\rm fp} \phi^l_{\rm fp} - \theta^s_{\rm tg}}{\sigma_\theta} \right]^2 .$$

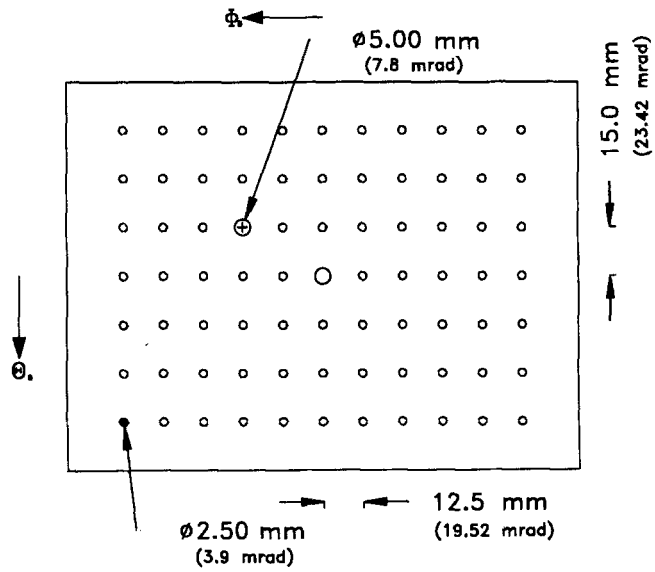

Fig. 17. Sieve slit of spectrometer A which contains 77 holes with a diameter of 2.5 mm except two holes close to the center which have 5 mm and are used to identify the orientation of the collimator.

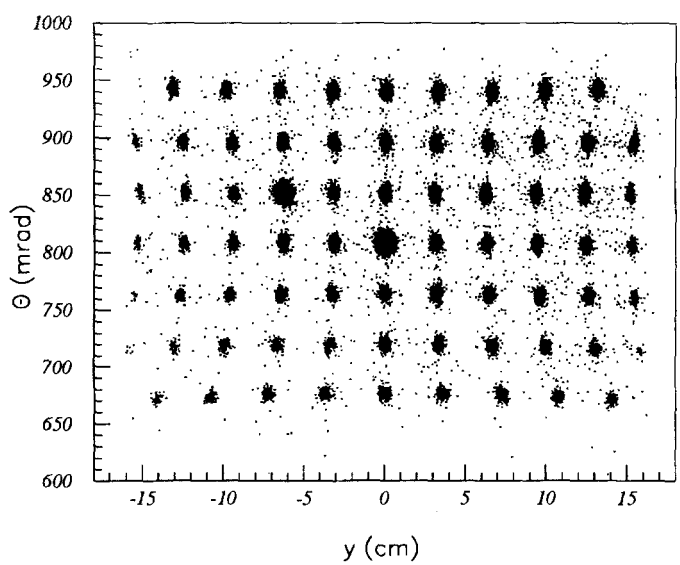

Fig. 18. Image of the sieve slit in spectrometer A in the θ_{fp}-y_{fp} spectrum.

Here s runs over all holes of the collimator and all events which lie within a certain range of the elastic peak and within a selected range of the image of the corresponding hole in the focal plane. This quantity is then minimized by varying the coefficients Q^{θ}_{jkl} which are to be determined. The same procedure gives the coefficients for $\phi_{\rm tg}$ and $y_{\rm tg}$. This is repeated for various field settings of the spectrometer (typically in steps of 2%) which positions the elastic peak at different values $x_{\rm fp}$. One can then determine the $x_{\rm fp}$ dependence of the coefficients Q^{q}_{jkl} and obtains the final coefficients $\langle q_{\rm tg}|x^i_{\rm fp}\theta^j_{\rm fp}y^k_{\rm fp}\phi^l_{\rm fp}\rangle$ which allows one to determine the trajectory coordinates $\theta_{\rm tg}, y_{\rm tg}$ and $\phi_{\rm tg}$ (Fig. 19).

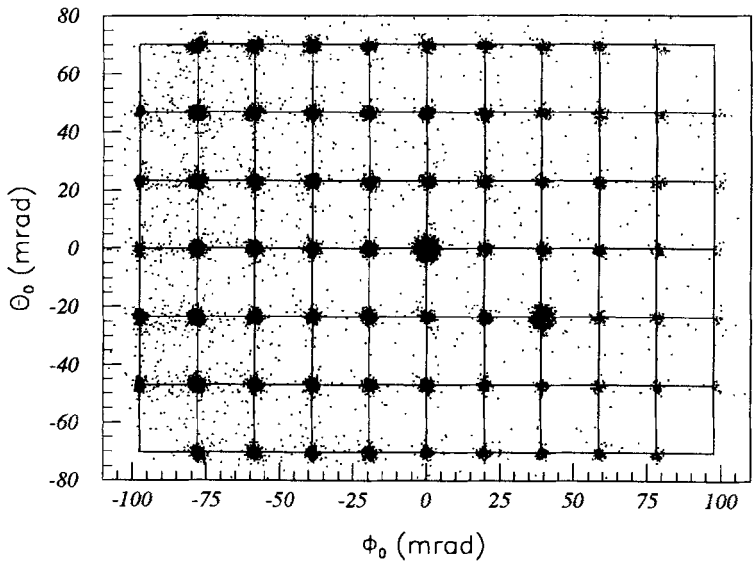

Fig. 19. Reconstructed image of the sieve slit of spectrometer A.

6.2 Determination of δ

A similar procedure as described above allows one to determine δ by minimizing the expression

$$\Delta p = \sum_s \left[\frac{\sum_{jkl} D_{jkl}\theta^j_{\rm fp}y^k_{\rm fp}\phi^l_{\rm fp} - x^s_{\rm fp}}{\sigma_x} \right]^2$$

which has to be done for an elastic peak but which does not require a sieve slit. The result of the complete vertex reconstruction can be illustrated in an elastic electron scattering spectrum of ^{12}C (Fig. 20–22). The large horizontal acceptance of spectrometer A produces a large kinematic broadening of the individual levels. Using the trajectory information from the focal plane, one can correct for aberrations

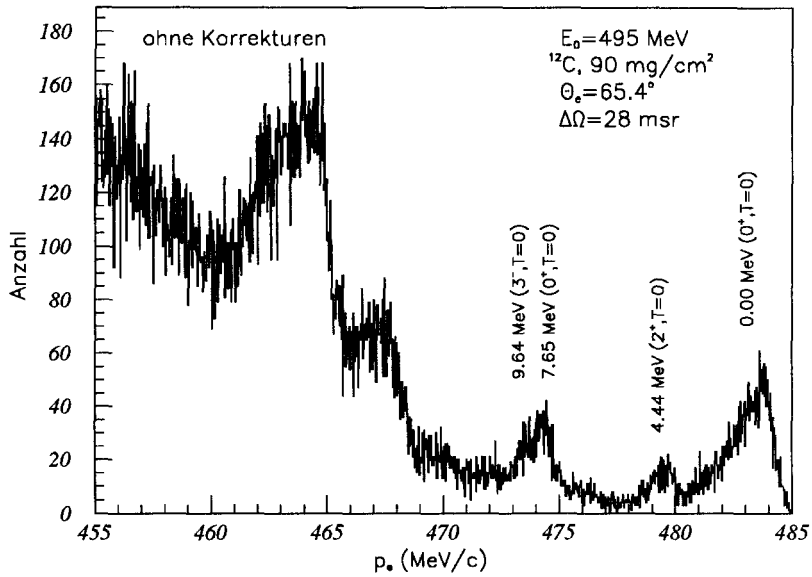

Fig. 20. Spectrum of electrons scattered off ^{12}C without any corrections.

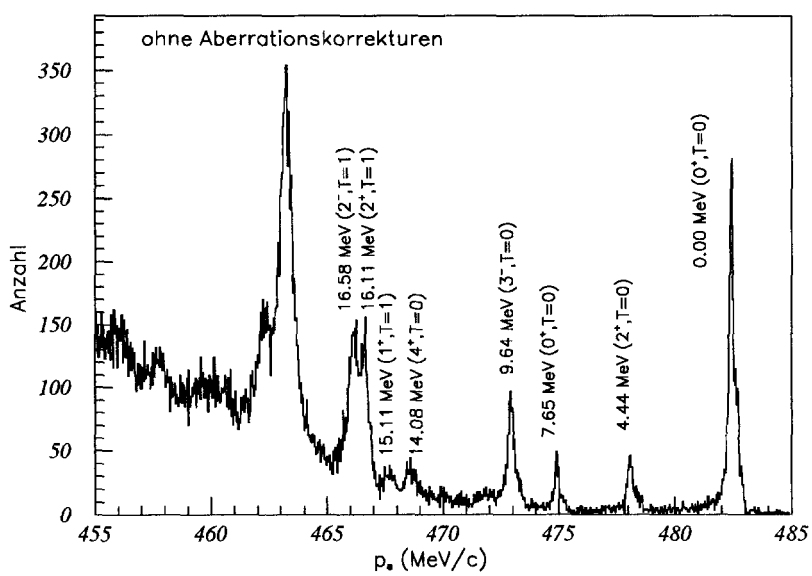

Fig. 21. Spectrum of electrons scattered off ^{12}C where the kinematic broadening has been corrected.

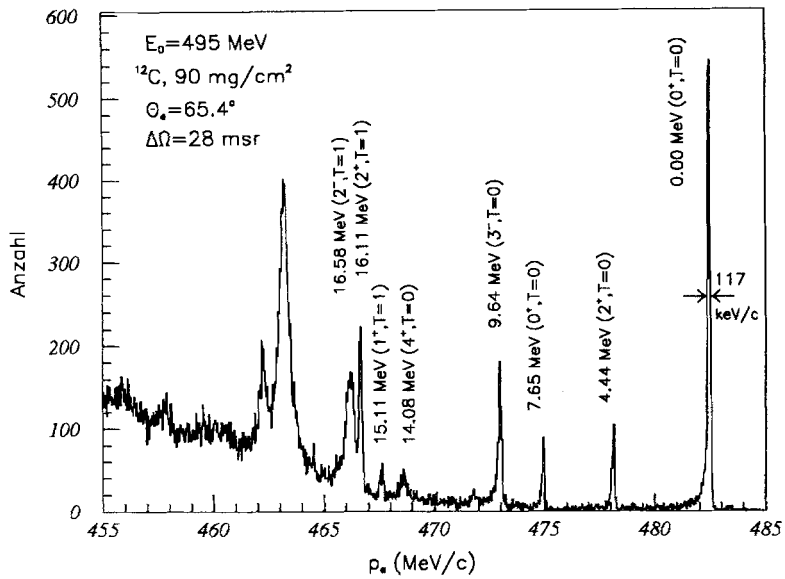

Fig. 22. Spectrum of electrons scattered off ^{12}C corrected for aberrations and kinematic broadening.

(described by the coefficients D_{ikl} above) and using the reconstructed scattering angles, it is possible to correct for the kinematic broadening.

Another possible procedure is to determine experimentally for each hole the central value for each of the focal plane coordinates. In a next step using these values in the ansatz for the transfer matrix, its elements are determined employing a fitting procedure. In this procedure one does not determine an x_{fp}-dependence of the Q_{jkl} coefficients but one directly fits all the coefficients $\langle\theta_{\rm tg}|x^i_{\rm fp}\theta^j_{\rm fp}y^k_{\rm fp}\phi^l_{\rm fp}\rangle$ for all settings in δ. A detailed discussion of the uniqueness and error analysis of these procedures can be found in reference [19].

6.3 Absolute momenta

In the above two sections I have discussed the determination of quantities with respect to the central (or reference) trajectory. In reality and especially in (e,e′p) reactions one needs to know absolute quantities, such as scattering angle and momenta. One usually knows the absolute position of the spectrometer very well and it is therefore not difficult to determine the absolute scattering angle for a particle. The determination of an absolute momentum, however, requires a determination of the spectrometer constant Γ which is defined as $p_{\rm ref} = \Gamma|\vec{B}|$. Γ can be obtained from elastic and inelastic electron scattering from different nuclei. One fits the position of the elastic peak and inelastic levels for different target nuclei and scattering angles. From this one can determine the spectrometer constant and the incident energy. If one repeats this procedures for several field settings and different inci-

dent energies it is also possible to determine the dependence of the spectrometer constant on the magnetic field. In this case the "constant" varies which can be a result of saturation effects at the edges of the magnet. In the case of spectrometer A the spectrometer "constant" is described by a 4th order polynomial in $\vec{B}$.

A spectrometer which is calibrated as discussed above is now capable to determine the four-momenta of incident electrons, protons and pions.

7 Two spectrometer coincidence

Two spectrometers which have been studied and optimized as discussed in the preceding section can now be combined in order to detect two particles which emerge from the same reaction in the target. In practice one measures the time between the arrival of the trigger signals in the two spectrometers which is called the time-of-flight (TOF) and should always be the same for particles from the same reaction. The observed TOF histogram shows a peak which is considerably wider than one would expect from the intrinsic time resolution of a plastic scintillator. The major contribution to the observed width arises from the different flight times of particles with different momenta (different velocities and different path lengths)

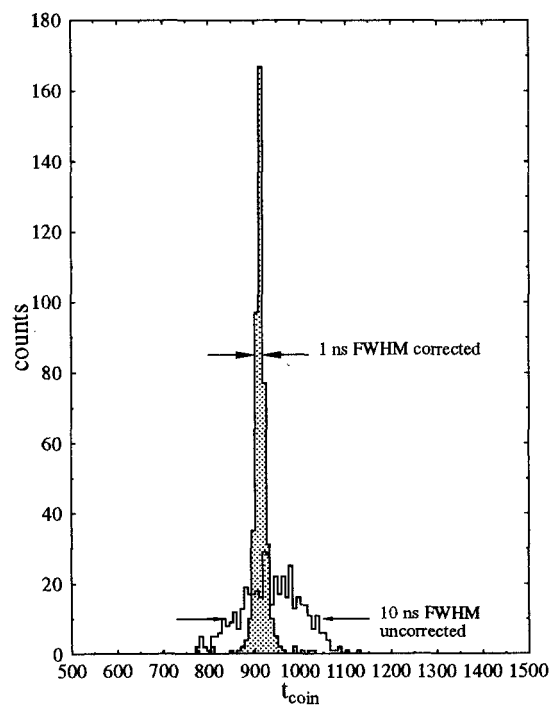

Fig. 23. Measured TOF spectrum of the D(e,e'p)n reaction at $p_{\text{miss}} = 0$. The solid line is the uncorrected spectrum with about 11.5 ns FWHM and the shaded area is the corrected spectrum with 0.75 ns FWHM.

between the target and the detector package. In addition the measured time also includes the time required by the light in the scintillator to arrive at the photocathode of the photomultiplier, its transit time and the time required by the detector electronics (amplifiers, discriminators, cables, coincidence units, delays etc.) to produce the necessary logical signal which can be used in the coincidence. All these effects contribute to the observed smearing of the measured time of flight (Fig. 23). Events from the target which originate from the different reactions (accidental coincidences) do not have a constant time relation and produce a constant continous background in the TOF spectrum. If the cross section of the investigated reaction is very small it is possible that the TOF spectrum is dominated by the accidentals and the signal of the coincidence reaction cannot be separated. It is therefore necessary to optimize the time resolution.

The correction of the time of flight contains the correction for the path length differences which are A typically ± 1.5 m for spectrometer. Path length differences can be described by a polynomial similar to the one used in the vertex reconstruction. The coefficients are determined by means of a fit which minimizes the width of the TOF peak. As before the starting values are obtained from the calculated optical properties of the spectrometer. In addition using the trajectory information

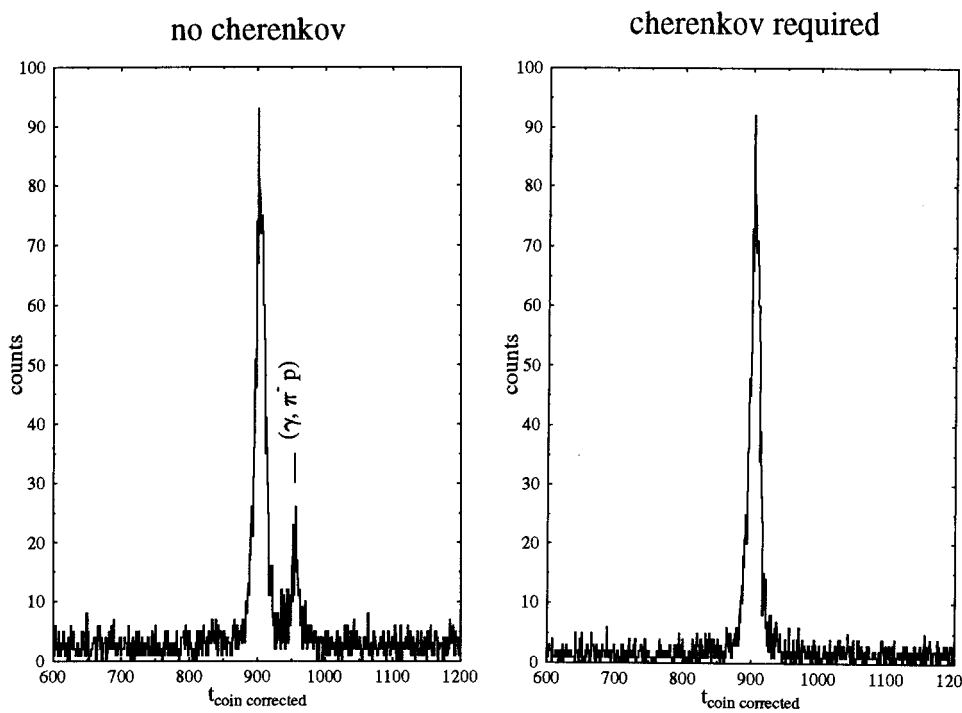

Fig. 24. D(e,e′p)n TOF spectrum at p_{miss}=750 MeV/c. The small peak in the left spectrum corresponds to γ, π^-p reactions which are absent if one requires a signal in the Cherenkov detector of the electron spectrometer.

provided by the VDC's, one can calculate the position where the particle crossed the scintillator and from this the 'time-of-flight' of the scintillation light to the photocathode of the photomultiplier. Each scintillator has also a certain offset which is included in the fit.

Including all this information in the correction function, one can reduce the width of the TOF peak from 11.5 ns to 0.75 ns (Fig. 23). This allows one to clearly identify true events even in a large background of accidental coincidences. A good time resolution makes it also possible to discriminate between different particle types. The TOF spectrum in Fig. 24 on the left side has two peaks. The smaller one on the right side corresponds to the reaction $D(\gamma, \pi^- p)p$ where the pions are detected in the electron spectrometer. If one demands a signal in the Cherenkov detector in the focal plane of the electron spectrometer the small peak vanishes while the large one which corresponds to the D(e,e′p)n reaction remains unchanged.

8 Momentum distribution of deuterium

In the last sections I have discussed the necessary equipment to perform a coincidence experiment between two spectrometers. In this chapter I will try to sketch the main steps in an analysis to extract a momentum distribution from raw data. The momentum distribution is in general not an observable but a model dependent quantity as I have mentioned in the introduction. For deuterium at relatively low missing momenta the final states interactions are relatively small and the PWIA is a reasonably good approximation.

8.1 Experimental details

Electron scattering from deuterium is performed using a liquid deuterium target. The liquid is circulated between the cylindrical target cell (diameter 2 cm) and a heat exchanger by means of a fan (Fig. 25). This spreads the energy deposited by the beam in a large enough volume of liquid to prevent local boiling and the correspondingly large variations in the luminosity. To further avoid local boiling (e.g. in the boundary layer of the cell walls) the beam has been rastered with a frequency of about 2 to 3 kHz over an area of 5×6 mm^2. The beam position has been measured on an event by event basis to completely reconstruct the reaction vertex and to correct for variations in the coordinate x_{tg}. The target thickness can be checked using elastic electron scattering and comparing the determined cross section to published data such as the ones measured at Saclay with high precision [21].

In this example we have used spectrometer B to detect electrons and the emerging protons have been detected in spectrometer A. Spectrometer B was at an angle of 45° and spectrometer A at an angle of 51.63°. Reconstructing the momentum vectors of the detected particles (electron and proton), one can determine the momentum transfer vector and from this using momentum conservation the missing momentum. From the measured energies using energy conservation one can calcu-

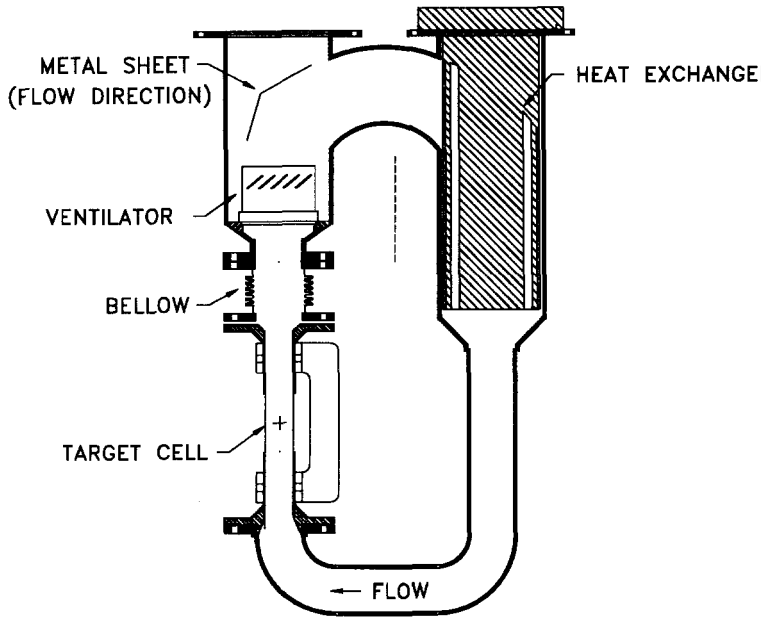

Fig. 25. Liquid deuterium/hydrogen target used at Mainz.

late the missing energy:

$$\begin{aligned} &\text{Momentum conservation:} \quad \vec{q} &&= \vec{p}_{\mathrm{f}} + \vec{p}_{\mathrm{miss}} \,. \\ &\text{Energy conservation:} \quad \epsilon_{\mathrm{m}} &&= \omega - T_{\mathrm{p}} - T_{\mathrm{r}} \,. \end{aligned}$$

In PWIA the magnitude of the missing momentum is equal to the magnitude of the initial momentum of the struck particle. The missing energy spectrum is used to select the specific reaction one wants to study. In the case of the D(e,e′p)n reaction the missing energy spectrum at energies below the pion production threshold should consist of only a single peak located at a missing energy which corresponds to the binding energy of the deuteron. In the missing energy spectrum shown in Fig. 26 one can clearly distinguish two peaks. One located at $\epsilon_{\mathrm{m}} = 0$ and the other at $\epsilon_{\mathrm{m}} = 2.225$ MeV. The first one corresponds to the ^{1}H(e,e′p) reaction from the hydrogen impurity in liquid deuterium. This process can be used for calibration purposes. In a heavier nucleus, however, the structure of the missing energy is much more complicated (or much richer depending on the point of view) which reflects the variety of possible final states of the residual nucleus. If one wants to determine the missing momentum distribution for a selected final state, one constructs a two dimensional spectrum in the variables ϵ_{m} and p_{miss}.

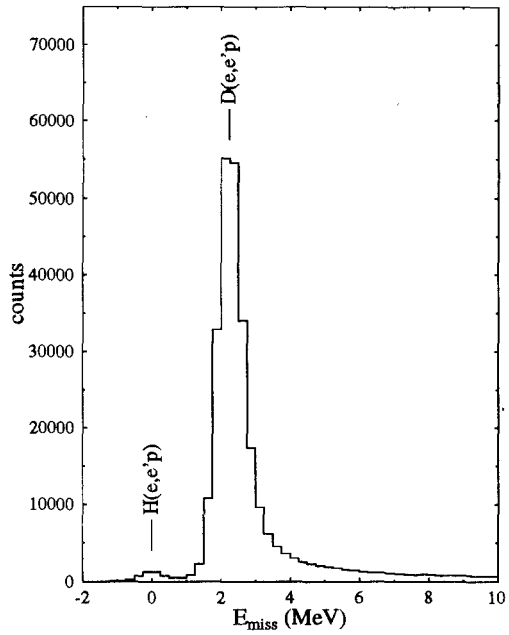

Fig. 26. Missing energy spectrum of the D(e,e'p)nreaction on the quasi elastic peak.

8.2 Phase space considerations

In a single arm experiment one determines a cross section as follows:

$$\frac{\mathrm{d}\sigma}{\mathrm{d}\Omega} = \frac{N_\mathrm{e}}{N_\mathrm{e}^\mathrm{inc} N_\mathrm{target}} A_\mathrm{target} \frac{1}{\Delta\Omega} \,.$$

This is possible if the solid angle for each bin in the single arm spectrum is the same. The second factor $1/\Delta\Omega$ can be interpreted as the phase space acceptance of the spectrometer for elastic scattering.

In a coincidence experiment the situation is more complicated because not each combination of the vectors k_μ^i, k_μ^f and p_μ^f which is allowed by the acceptances of the spectrometers, can contribute to a selected bin in the $\epsilon_\mathrm{m}/p_\mathrm{miss}$-spectrum. One has therefore first to calculate the phase space acceptance at the settings used to measure the $\epsilon_\mathrm{m}/p_\mathrm{miss}$-spectrum for each bin of the spectrum. This corresponds to an integral for each bin of the type:

$$V_\mathrm{B} = \int_{\Delta x_1,\ldots,\Delta x_6} s(x_1,\ldots,x_6)\mathrm{d}x_1 \cdots \mathrm{d}x_6 \,,$$

where V_B is the phase space volume for bin B, $x_1,\ldots,x_6$ are 6 kinematical variables such as $\omega, \vartheta_\mathrm{e}, \varphi_\mathrm{e}, p_\mathrm{f}, \theta_\mathrm{p}$ and φ_p. The function $s(x_1,\ldots,x_6)$ is the detection efficiency for a certain combination of the quantities $x_1,\ldots,x_6$ which feed bin B. In an ideal case one has $s = 1$ if the event lies within the acceptance of the spectrometers and

$s = 0$ otherwise. Values between 0 and 1 are possible if one knows the detection efficiency of the individual spectrometers (e.g. from measurements) as a function of the corresponding variables $x_1, \ldots, x_6$. This integral can be solved analytically for very simple cases only and in most practical applications one has to use Monte Carlo techniques to determine it.

This is usually done by randomly selecting a set of values $x_1, \ldots, x_6$ which lie within a hypercube with a volume given by $\Delta x_1 \cdots \Delta x_6$. This hypercube is chosen such that it completely contains the phase space volume of the experimental setup. As an example one can choose $\theta_e(= x_2)$ and $\phi_e(= x_3)$ in order to define the electron direction in spherical coordinates and $\theta_p(= x_4)$ and $\phi_p(= x_5)$ to define the proton direction. With the knowledge of the incident beam energy $\omega(= x_1)$ defines the electron momentum and $p_f(= x_6)$ defines the corresponding proton momentum. The values $\Delta x_2 \Delta x_3$ define the electron solid angle and Δx_1 describes the momentum acceptance of the electron spectrometer. The remaining quantities describe the proton spectrometer acceptance in the same way. By selecting a point in this hypercube, one has selected a coincidence event for which one calculates the relevant kinematic quantities such as missing energy ϵ_m and missing momentum p_{miss} or other quantities which are of interest for the specific reaction studied.

An additional advantage of the Monte Carlo method is that one can simulate different experimental conditions and their influence on the phase space acceptance very well. It is possible to simulate the effect of an extended target by varying the reaction vertex or one can take into account energy loss and multiple scattering processes of the emerging particles in the target and in the vacuum windows of the scattering chamber and the spectrometer entrance. Inefficiencies of the detector package can also be simulated if one determines the trajectories in the focal plane given the ones at the spectrometer entrance.

In conclusion the Monte Carlo method allows one to model the experiment very exactly. This makes it possible to determine the actual phase space acceptance of the selected experimental setup. As an example Fig. 28 shows the phase space for the D(e,e′p)n reaction taken at the settings of Table 4. From the spectrum in Fig. 28 one can clearly see that there are no sharp boundaries in the phase space acceptance but it gradually reaches zero at the edges. To correct the measured spectrum for the phase space acceptance the two spectra are divided by each other bin by bin. For this calculation one does not use the whole acceptance since this would produce large fluctuations in the bin which lie in the boundary region. There the statistical uncertainties in the experimental data are large and would even further be blown up by the correction. The boundary region of the calculated phase space acceptance is also very sensitive to the fine details of the treatment of multiple scattering and energy-loss processes and to a very precise knowledge of the edges of the spectrometer acceptances. Therefore one restricts the used phase space to a region where it is larger than typically 25% of its maximum value. The result of this procedure is presented in Fig. 27.

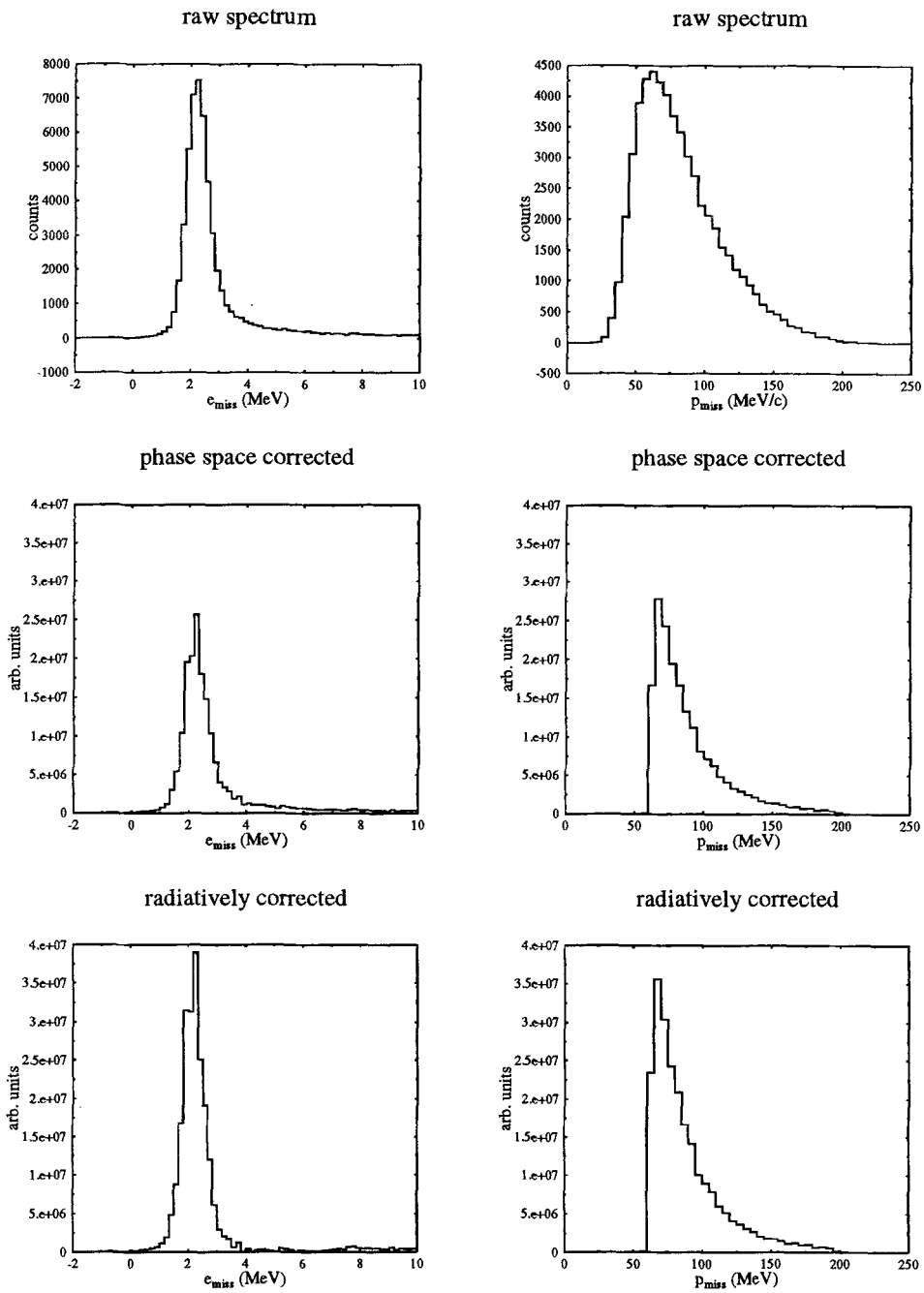

Fig. 27. Experimental ϵ_m and p_{miss}-spectra at different stages of the analysis (raw (top), corrected for phase space acceptance (middle) and radiatively unfolded (bottom)).

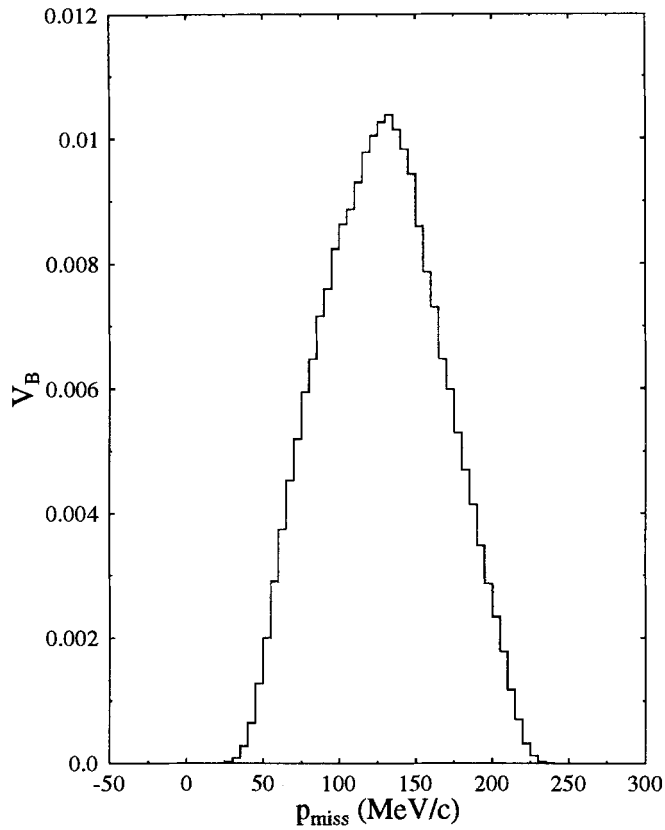

Fig. 28. Calculated phase space acceptance for the p_{miss}-spectrum.

Table 4. Kinematic settings for the spectrum shown in Fig. 28.

	Spectrometer A	Spectrometer B
Particles	protons	electrons
Angle (deg)	59.84	45.0
Reference momentum (MeV/c)	602.2	656.19
Momentum acceptance (MeV/c)	120	75
Horizontal angular acceptance (mr)	± 75	± 20
Vertical angular acceptance (mr)	± 70	± 70

8.3 Radiative corrections

Due to their small mass, electrons can easily radiate photons in the field of the target nuclei. The angular distribution of the emitted photons is strongly peaked in the direction of the incident and emerging electrons. In most calculations of corrections due to these processes one assumes that all photons are emitted in the direction of the momentum of the radiating particles (peaking approximation). An electron can emit a real photon in the field of the same nucleus in which the reaction takes place (internal Bremsstrahlung) or in the field of another nucleus (external Bremsstrahlung). The emission of real photons changes the kinematics at the interaction vertex. If the photon energy is larger than the energy bin size ΔE events which correspond to a certain bin are moved into another one and produce thereby a radiative tail. If the photon energy E_γ is smaller than the bin size ΔE, the result is just a redistribution of events within one bin. Emission and reabsorbtion of virtual photons produce an overall change of the cross section but do not produce a radiative tail. The correction due to internal Bremsstrahlung and the emission and reabsorption of virtual photons has been first calculated by Schwinger [22]. External Bremsstrahlung has been calculated by Bethe and Heitler [23]. Both calculations have later been refined to be applied to different scattering reactions [24–27]. Using these calculations, the experimentally determined spectra have to be corrected for these processes in order to be compared to theoretical calculations. Alternatively one could fold the theoretical calculations with the radiative processes. In order to correct the experimental ϵ_m/p_{miss}-spectrum for radiative processes an unfolding procedure has been used which has been developed in reference [28]. This method is based on the unfolding procedure described by Crannell *et al.* [29]. One considers the contents of each bin B as an elastic peak with a resolution which corresponds to the bin width. For this bin the correction due to radiative losses (Schwinger corrections, external Bremsstrahlung) is calculated. Using the corrected bin contents, the contributions to bins with lower energy (higher excitation energy) is calculated and subtracted. This procedure is repeated for each bin, starting with the bin of highest energy (lowest excitation energy). In the case of the ϵ_m/p_{miss}-spectrum the correction is more complicated since one has to take into account two radiative tails (or three if one includes the possibility of radiation of the emerging proton). An additional problem arises from the fact that one has to reconstruct the kinematics of each event which contributes to a bin in the ϵ_m/p_{miss}-spectrum. This information, however, is not available anymore and one has to use approximations to reconstruct averaged kinematics for the calculation of the radiative tails.

The result of the unfolding procedure of our ϵ_m/p_{miss}-spectrum corresponds essentially to the radiatively corrected (e,e′p) cross section. This spectrum (Fig. 27c) can now be used to determine the final momentum distribution $\rho(p_{miss})$. The last necessary step consists in dividing by the expression $k\sigma_{ep}$ (see the introduction), which has been averaged for each bin of the ϵ_m/p_{miss}-spectrum over the acceptance of the two spectrometers. After this division the missing momentum distribution is obtained by fitting the ϵ_m-spectrum corresponding to one (or more) bin(s) in p_{miss}.

Note that in the above expressions the coincidence cross section was always differential in the variables which have defined the hypercube enclosing the phase space acceptance. If the desired cross section has to be differential in other variables (e.g. ϵ_m), one has to calculate the averaged Jacobian for each bin of the ϵ_m/p_{miss}-spectrum and transform the experimental spectrum accordingly.

9 Experimental spectral functions for D, ^{12}C and ^{16}O

In the preceding sections I have described the equipment and the basic steps of the analysis in order to obtain cross sections and momentum distributions of nuclei using the (e,e′p)-reaction. In this section I will now present as an illustration some selected results from (e,e′p) experiments. Since my focus in these lectures was to give an overview over the experimental techniques and methods employed to determine coincidence cross sections, I will present a few selected examples of perfomed experiments only.

9.1 Experiments on deuterium

In nuclear physics, deuterium plays a similar role as the hydrogen atom in atomic physics. As a two body system all the complications related to many-body effects are absent. This allows one to study a bound state of the strong interaction with very small theoretical uncertainties. In the past fundamental properties of the strong interaction were discovered in experiments on this simple system. For example the value of the measured electric quadrupole moment can only be explained if the ground state of the deuteron consists of a mixture of an S- and a D-state with both nucleon spins aligned. A mixture of an S- and a D-state can only be produced by a noncentral part of the NN interaction. This ground state wave function also gives the correct magnetic moment where the deviation from the value obtained with a pure S-state deviates by -2.6% only. That this small deviation can be explained clearly shows the advantage of having a simple system. From electron scattering from deuterium one has found large contributions from meson exchange currents [30] and also contributions from isobar cofigurations where one of the nucleons is virtually excited. In PWIA the (e,e′p)-reaction directly probes the momentum distribution of deuterium which is the Fourier transform of its wave function. If one determines this quantity at increasing missing momenta, one probes shorter and shortes distances in a PWIA world. This investigation has been started at Saclay where the momentum distribution has been measured up to missing momenta of 350 MeV/c (Fig. 29) [41]. Cross sections have also been determined for missing momenta up to 500 MeV/c [42]. These measurements used momentum transfers of 279, 350 and 450 MeV/c. At missing momenta around 300 MeV/c the momentum distribution should be dominated by the D-state wave function. Unfortunately at these values of missing momenta and the relatively small momentum transfer, PWIA is not valid anymore and FSI contribute heavily to the cross section which makes the simple interpretation impossible. In a first experiment at MAMI we have determined the momentum distribution at a momentum

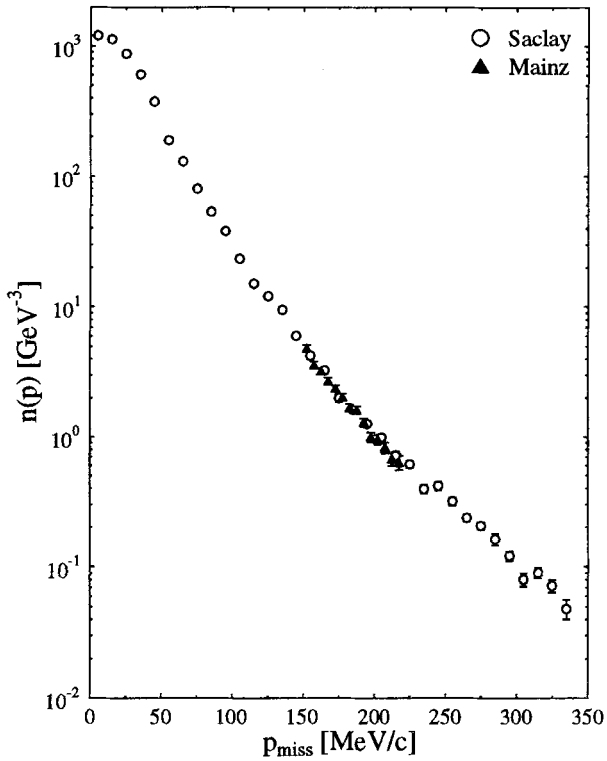

Fig. 29. Momentum distribution of deuterium as measured in Saclay [41] for $p_{\rm miss} \leq$ 300 MeV/c compared with data taken at the same kinematics at MAMI.

transfer of 600 MeV/c up to missing momenta of 930 MeV. A very preliminary result is presented in Fig. 30. It is interesting that the momentum distribution is relatively flat between missing momenta of 500 MeV/c and 850 MeV/c and seems to fall again for higher missing $p_{\rm miss}$. It is clear that more data have to be taken in order to fill the gaps in the data and to verify the observed tendencies. Another important experimental task is to determinate of the individual response functions. The longitudinal response function is hardly affected by processes such as MEC and IC while the transverse is highly sensitive. Therefore the longitudinal response function should be well suited to explore details of the deuteron wave function while the transverse one can be used to investigate non-nucleonic contributions. Separations at small missing momenta have been performed at NIKHEF [31,32] and Saclay [33]. In all experiments the longitudinal and the transverse response functions have been separated in parallel kinematics ($\vec{p}_{\rm miss}$ parallel (antiparallel) to $\vec{q}$). The measurement of response functions is considerably more complex than the determination of a momentum distribution since one has to measure absolute cross sections and is much more sensitive to systematic errors. The problem of separating response functions in measurements with large kinematic acceptances has

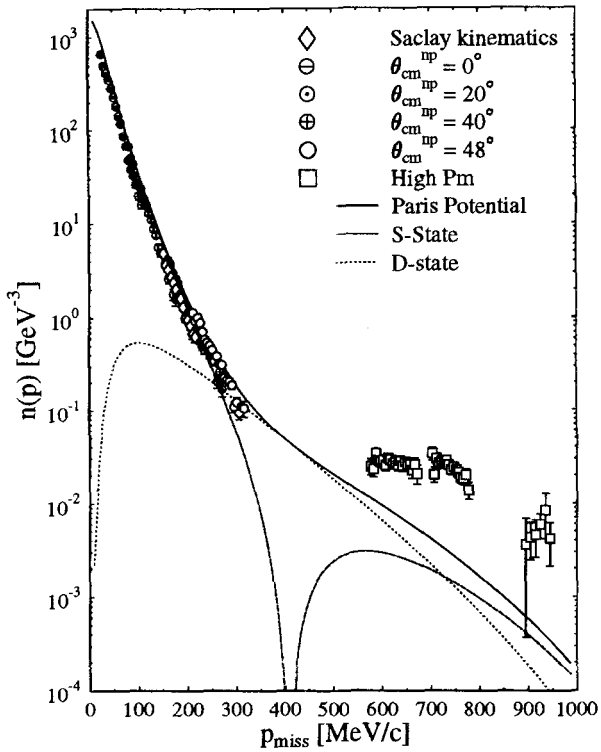

Fig. 30. Preliminary deuterium momentum distribution measured in Mainz.

been studied in reference [34] where a possible method is proposed to extract these response functions in a model independent way. The determination of individual response functions in coincidence experiments is a major part of the experimental program in Mainz.

9.2 Experiments on ^{12}C and ^{16}O

While the missing energy spectrum of deuterium consisted of a single peak at its binding energy, the corresponding spectrum for a more complex nucleus, such as carbon or oxygen, is considerably more complicated (Fig. 31) and can also be interpreted as the excitation spectrum of the residual system. At BATES the missing energy spectrum for ^{12}C has been studied for missing energies up to 300 MeV [35–37] including a longitudinal transverse separation [38]. These experiments showed that there are reaction mechanisms which contribute to the (e,e′p) cross section that produce considerable strength at large missing energies. In this missing energy region, the momentum transfer is not absorbed by a single proton but by a correlated pair. As a consequence two nucleons are knocked out of the nucleus. Also processes where three nucleons are knocked out are possible as has been shown in a calculation by Takaki [39]. Momentum distributions for ^{12}C have been determined at Saclay [40]

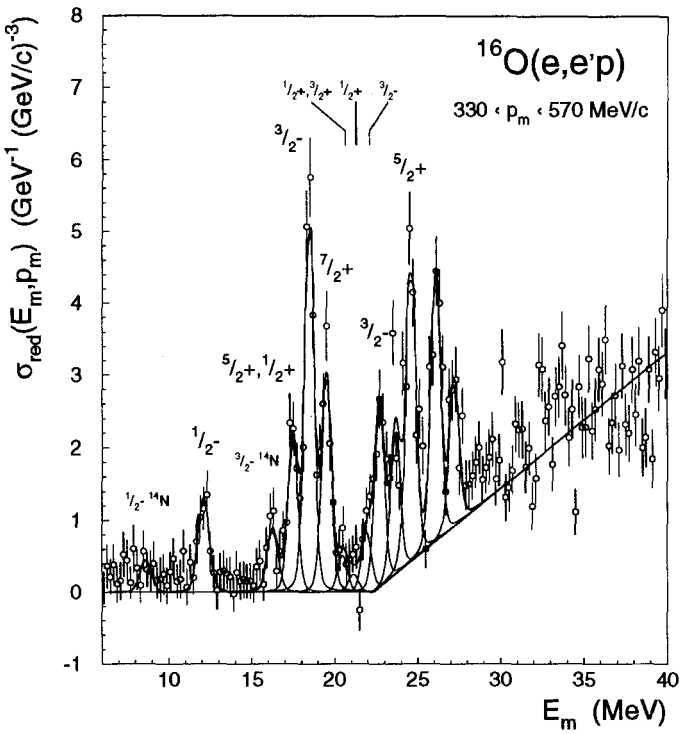

Fig. 31. Missing energy spectrum for ^{16}O at $p_{\mathrm{miss}} = 450$ MeV/c.

and at NIKHEF [44]. From the momentum distributions of bound states spectroscopic factors have been determined which are a measure of the occupancy of a certain single particle state. These experiments allow one to test how well one can describe a nucleus within the framework of the independent particle shell model. The interpretation of (e,e'p) data along these lines are not model independent. Especially it is important to be able to take final state interactions into account. This is usually done by means of an optical potential which is used to describe the final state of the struck proton. These potentials have been determined from proton scattering experiments and it is not completely clear how well they describe a proton moving inside the nucleus. There exist several reviews on these experiments [45] and their interpretation. Using the possibilities of the new spectrometers in combination with the CW-beam we have studied the (e,e'p)-reaction on ^{16}O up to missing momenta of 700 MeV/c and missing energies of 200 MeV. In Fig. 32 a series of missing energy spectra for increasing missing momenta is presented. One can clearly see how the strength above 20 MeV increases with increasing missing momentum until it completely dominates the spectrum. As in the MIT experiment at low missing momenta, the strength at high missing energies can be seen but is not very prominent compared to the same spectrum taken at missing momenta

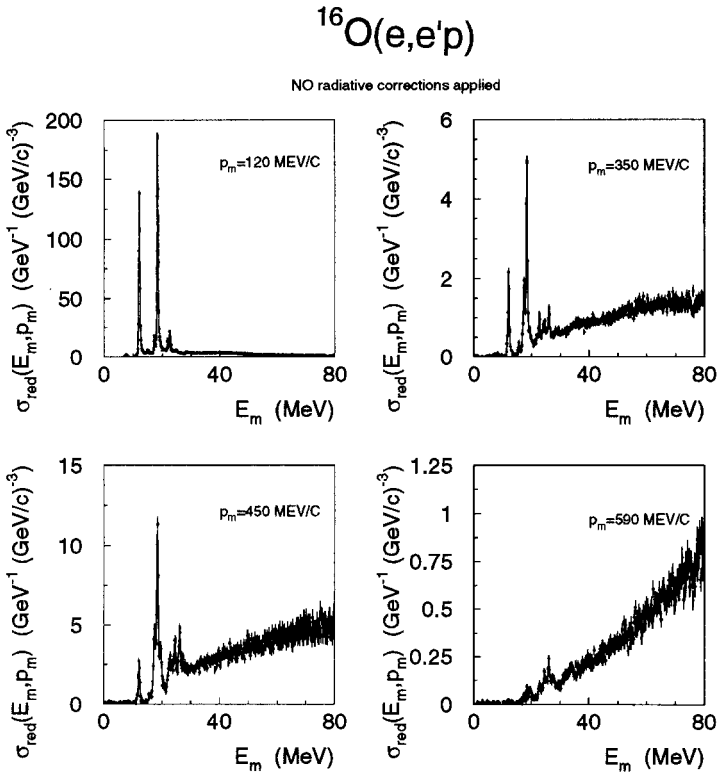

Fig. 32. Recently measured missing energy spectra for oxygen taken at increasing missing momenta.

above 350 MeV/c. A similar phenomenon has been observed ^{3}He [43]. There a broad "peak" was observed in the continuum which could be explained by breaking up a deuteron within the ^{3}He nucleus. Similarly we expect two or more nucleons being knocked out at these high missing energies. In Fig. 33 I show the missing momentum distribution for proton knock out from the $1p_{1/2}$ and the $1p_{3/2}$ valence orbitals. The solid lines show calculations using an optical potential. The deviations from the data require further studies with different optical potentials. The optical potentials which are currently available have been determined at smaller proton kinetic energies compared to the kinetic energies of the emerging protons. Using the same optical potential, we could describe the data at lower missing momenta which have been taken at a kinematic setting which is very close to the one measured previously at NIKHEF. The spectroscopic factors determined from these measurements are in agreement with the ones determined at NIKHEF. Therefore the deviations observed at higher p_{miss} could be attributed to the inadequacy of the optical potential used for these high energies. These data are accepted for publication [46].

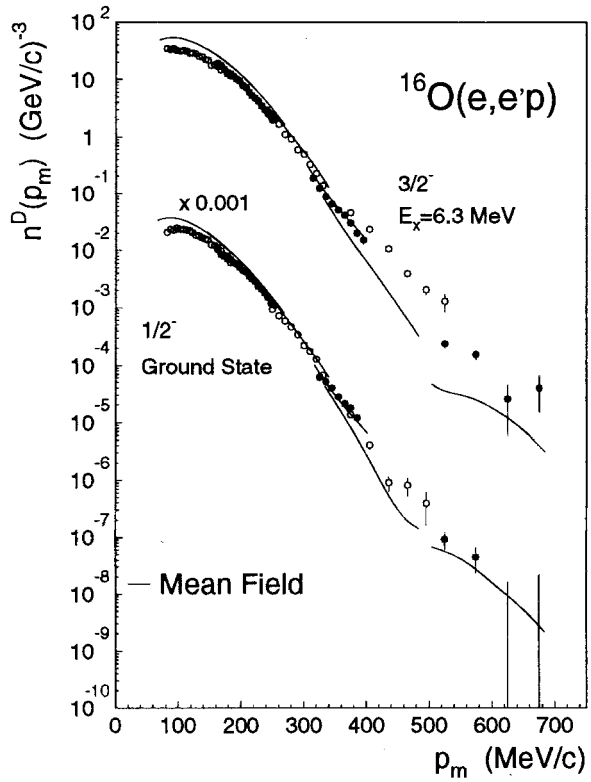

Fig. 33. Reduced cross section (momentum distribution in PWIA) for proton knock out of the $1p_{1/2}$ and the $1p_{3/2}$ shells.

10 Conclusion

I have described the experimental equipment used in Mainz at the MAMI facility to perform coincidence experiments with electrons using spectrometers. As an example I have selected the determination of the momentum distributions of deuterium and of the $p_{1/2}$ and $p_{3/2}$ states in oxygen. Other experiments on pion production can also be performed. For instance, one can measure the electroproduction of charged pions in order to study the different reaction mechanisms and to test low energy theorems or one studies the electroproduction of neutral pions in order to test predictions from chiral perturbation theory. In another experiment using a spectrometer in coincidence with a neutron detector one can measure by comparing D(e,e′n)p and D(e,e′p)n reactions the magnetic formfactor of the neutron. In addition using a polarimeter in the focal plane of a spectrometer one can determine the polarization of the ejected proton. In reference [47] this subject has been discussed in the same school in 1993. One can also use polarized targets such as ^{3}He in combination with a spectrometer and a neutron detector to study

the electric formfactor of the neutron. These examples should illustrate the wide variety of different subjects that can be investigated using coincidence reactions with electrons. All these experiments become feasible with the availability of new CW-accelerators which make the available high intensities usable for coincidence experiments.

References

[1] Dieperink A.E.L. and De Forest T., jr.: Ann. Rev. Nucl. Sci. *25* (1975) 1.
Frullani S. and Mougey J.: Adv. Nucl. Phys. *14* (1984).

[2] Boffi S., Giusti C. and Pacati F.D.: Phys. Rep. *226* (1993) 1.

[3] Giusti C. and Pacati F. D.: Nucl. Phys. A *473* (1987) 717; *485* (1988) 461.

[4] De Forest T., jr.: Nucl. Phys. A *392* (1983) 232.

[5] Herminghaus H. et al.: *in* Proc. LINAC Conf. 1990, Albuquerque, New Mexico.
Herminghaus H. et al.: Nucl. Instrum. Meth. *138* (1976) 1.

[6] Grunder H.: *in* Proc. 1988 Linear Accelerator Conf., CEBAF 1988.

[7] MIT Linac Group, MIT Summer Studies (Ed. W. Bertozzi and S. Kowalski), TID-24667 (1967) 17.

[8] De Vries C., De Jager C.W., Lapikàs L., Luijckx G., Maas R., De Vries H., and De Witt Huberts P.K.A.: Nucl. Instrum. Meth. *223* (1984) 1.

[9] Luijcks G. et al.: *in* Proc. 1989 IEE Particle Accelerator Conf., Chicago 1989, p. 46.

[10] Pulse Strtcher Ring: Proposal for a CW Upgrade, Bates Linear Accelerator Center, MIT.

[11] Saskatchewan Accelerator Laboratory Annual Report 1991.

[12] Brown K.L.: "First and Second Order Charged Particle Optics". Lecture given at the BNL Accelerator Physics Summer School, July 1983.

[13] Spencer J.E. and Enge H.A.: Nucl. Instrum. Meth. *49* (1967) 181.
Enge H.A. and Kowalski S.: *in* 3rd Int. Conf on Magnet Technology, 1970, p. 103.

[14] Brown K.L., Carey D.C., Iselin C., and Rothacker F., TRANSPORT: A Computer Program For Designing Charged Particle Beam Transport Systems, Stanford Linear Accelerator Center (1991) SLAC(91), NAL-91, and CERN-73-16.

[15] Carey D.C., TURTLE: A Computer Program For Simulating Charged Particle Beam Transport Systems. NAL-64, Fermilab National Accelerator Laboratory, 1978.

[16] A1 Collaboration: Many colleagues have contributed to the realization of the three-spectrometer setup and are involved in the physics programme. This is illustrated by the following list of A1 collaborators:
W. Bertozzi[12], L. de Bever[3], K.I. Blomqvist[1], W.U. Boeglin[1], R. Böhm[1], E. Brash[4], J.R. Calarco[2], J.P. Chen[12], D. Dale[12], O. Denhard[1], M. Distler[1], R. Edelhoff[1], A. Felthman[3], R. Florizone[12], J. Friedrich[1], D. Fritschi[3], R. Geiges[1], S. Gilad[12], R. Gilman[4], P. Gitzel[1], C. Glashausser[4], F. Heinemann[1], M. Jones[4], J. Jourdan[3], M. Kahrau[1], M. Klein[1], M. Korn[1], H. Kramer[1], K.W. Krygier[1], V. Kunde[1],

M. Kuss[5], J. Lác[4], J.M. Laget[6], A. Liesenfeld[1], M. Loppacher[3], G. Masson[3], K. Merle[1], C.L. Morris[7], R. Neuhausen[1], E.A.J.M. Offermann[1], Th. Pospischil[1], M. Potokar[8], C. Rangacharyulu[9], R.D. Ransome[4], A. Rokavec[8], A. Richter[5], A.W. Richter[1], B.G. Ritchie[10], S. Robinson[3], G. Rosner[1], P. Rutt[4], P. Sauer[1], A. Sarty[12], S. Schardt[1], C.G. Schilling[1], J.P. Schiffer[11], G. Schrieder[5], Ch. Schrimpf[1], I. Sick[3], M.D. Solano Ros[1], Ph. Steiner[3], P. Trüb[3], Th. Veit[1], B. Vodenik[8], A. Wagner[1], Th. Walcher[1], W. Wilhelm[1], S. Wolf[1], M. Yadav[4], B. Zihlmann[3].

[1]Institut für Kernphysik, Universität Mainz, D-55099 Mainz; [2]Department of Physics, University of New Hampshire, Durham, USA; [3]Institut für Physik, Universität Basel, CH-4056 Basel; [4]Physics Department, Rutgers University, Piscataway, USA; [5]Institut für Kernphysik, TH Darmstadt, D-64289 Darmstadt; [6]CEN Saclay, France; [7]LAMPF, LANL, Los Alamos, USA; [8]Institut "Jožef Stefan", University of Ljubljana, Slovenia; [9]University of Saskatchewan, Saskatoon, Canada; [10]Physics Department, Arizona State University, Tempe, USA; [11]Physics Department, ANL, Argonne, USA; [12]Massachusetts Institute of Technology, Cambridge, USA.

[17] A1 Collaboration: Mainz Annual Report 1992–1993. Institut für Kernphysik, Universität Mainz, p. 17.

[18] Bertozzi W. et al.: Nucl. Instrum. Meth. *141* (1977) 457.

[19] Veit Th., Friedrich J., and Offerman E.A.J.M.: Nucl. Instrum. Meth. A *336* (1993) 572.

[20] Offerman E.A.J.M., De Jager C.W., and De Vries H.: Nucl. Instrum. Meth. A *262* (1987) 298.

[21] Platchkov S., Amroun A., Auffret S., Cavedon J.M., Dreux P., Duclos J., Frois B., Goutte D., Hachemi H., Martino J., and Phan X.H.: Nucl. Phys. A *510* (1990) 740.

[22] Schwinger J.: Phys. Rev. *76* (1949) 790.

[23] Bethe H.A. and Heitler W.: Proc. Roy. Soc. A *146* (1943) 83.

[24] Maximon L.C.: Rev. Mod. Phys. *41* (1969) 193.

[25] Mo L.W. and Tsai Y.S.: Rev. Mod. Phys. *41* (1969) 205.

[26] Borie E. and Drechsel D.: Nucl. Phys. A *167* (1971) 369.

[27] Friedrich J.: Nucl. Instrum. Meth. *129* (1975) 505.

[28] Quint E.: Dr. Thesis, University of Amsterdam, 1988.

[29] Crannell H.: Nucl. Instrum. Meth. *71* (1969) 208.

[30] Auffret S. et al.: Phys. Rev. Lett. *46* (1985) 1362.
Lee K.S. et al.: Phys. Rev. Lett. *67* (1991) 2634.

[31] Van der Schaar M. et al.: Phys. Rev. Lett. *66* (1991) 2855.

[32] Van der Schaar M. et al.: Phys. Rev. Lett. *68* (1992) 776.

[33] Ducret J.E. et al.: Phys. Rev. C *49* (1994) 1783.

[34] Veit Th. et al.: Z. Phys. A *349* (1994) 161.

[35] Lourie R.W. et al.: Phys. Rev. Lett. *56* (1986) 2364.

[36] Weinstein L.B., et al.: Phys. Rev. Lett. *64* (1990) 1664.

[37] Baghaei H. et al.: Phys. Rev. C *39* (1989) 177.

[38] Ulmer P.E. et al.: Phys. Rev. Lett. *59* (1987) 2259.

[39] Takaki T.: Phys. Rev. Lett. *62* (1989) 395.

[40] Mougey J. et al.: Nucl. Phys. A *262* (1976) 461.

[41] Bernheim M. et al.: Nucl. Phys A *365* (1981) 349.

[42] Turck-Chieze S. et al.: Phys. Lett. B *142* (1984) 145.

[43] Marchand C. et al.: Phys. Rev. Lett. *60* (1988) 1703.

[44] Van der Steenhoven G. et al.: Nucl. Phys. A *480* (1988) 547.

[45] De Witt Huberts P.K.A.: J. Phys. C *16* (1990) 507.

[46] Bloqvist K.I. et al.: Phys. Lett. B (in press).

[47] Offerman E.A.J.M: Czech. J. Phys. *43* (1993) 387.